

3-10-2010

Thermal Neutron Point Source Imaging using a Rotating Modulation Collimator (RMC)

Nathan O. Boyce

Follow this and additional works at: <https://scholar.afit.edu/etd>

 Part of the [Elementary Particles and Fields and String Theory Commons](#), [Nuclear Commons](#), and the [Optics Commons](#)

Recommended Citation

Boyce, Nathan O., "Thermal Neutron Point Source Imaging using a Rotating Modulation Collimator (RMC)" (2010). *Theses and Dissertations*. 2178.
<https://scholar.afit.edu/etd/2178>

This Thesis is brought to you for free and open access by the Student Graduate Works at AFIT Scholar. It has been accepted for inclusion in Theses and Dissertations by an authorized administrator of AFIT Scholar. For more information, please contact richard.mansfield@afit.edu.



**THERMAL NEUTRON POINT SOURCE IMAGING USING A ROTATING
MODULATION COLLIMATOR (RMC)**

THESIS

Nathan O. Boyce, 2d. Lt., USAF

AFIT/GNE/ENP/10M-01

**DEPARTMENT OF THE AIR FORCE
AIR UNIVERSITY**

AIR FORCE INSTITUTE OF TECHNOLOGY

Wright-Patterson Air Force Base, Ohio

APPROVED FOR PUBLIC RELEASE; DISTRIBUTION UNLIMITED

The views expressed in this thesis are those of the author and do not reflect the official policy or position of the United States Air Force, Department of Defense, or the U.S. Government.

AFIT/GNE/ENP/10M-01

THERMAL NEUTRON POINT SOURCE IMAGING USING A ROTATING
MODULATION COLLIMATOR (RMC)

THESIS

Presented to the Faculty

Department of Engineering Physics

Graduate School of Engineering and Management

Air Force Institute of Technology

Air University

Air Education and Training Command

In Partial Fulfillment of the Requirements for the
Degree of Master of Science in Nuclear Engineering

Nathan O. Boyce, BS

2d. Lt., USAF

March 2010

APPROVED FOR PUBLIC RELEASE; DISTRIBUTION UNLIMITED


AFIT/GNE/ENP/10M-01

THERMAL NEUTRON POINT SOURCE IMAGING USING A ROTATING
MODULATION COLLIMATOR (RMC)

Nathan O. Boyce, BS


2d. Lt., USAF

Approved:



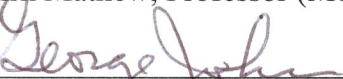
Benjamin R. Kowash, Captain, USAF (Chairman)

12 Mar 2010
Date



Kirk Mathew, Professor (Member)

12 Mar 2010
Date



George John, Professor Emeritus (Member)

16 Mar 2010
Date

Abstract

This thesis demonstrates a previously untested capability of the Rotating Modulation Collimator (RMC) to image a point-like neutron source. The encouraging results, achieved using low-energy neutrons, provide motivation for further refinement and continued research with higher-energy neutrons. The detector and the masks on an existing RMC imaging system were exchanged to function with neutrons. The source in this research produced a poly-energetic spectrum ($E_{\text{avg}} = 4.6 \text{ MeV}$) of neutrons through the ${}^9\text{Be}(\alpha, n){}^{12}\text{C}$ reaction. The source of alpha particles was a 72.7 mCi (as of 22 Sep 61) ${}^{239}\text{Pu}$ source. The RMC detector was located 250 cm from the bare source and operated for three hours to generate a modulation profile: The number of particles detected at each rotation angle of the masks – it is unique for each source location.

The measured modulation profiles were used in a Maximum-Likelihood-Expectation-Maximization algorithm to reconstruct the images, and a Bootstrap resampling technique was used to determine uncertainty. The reconstructed images exhibited high contrast but low precision. The resampled image locations were widely distributed, but the most frequent value was very accurate. The uncertainty originated from an expectation model that did not account for fast neutron downscatter into the thermal neutron region as well as the fast neutrons streaming through the masks and being detected.

Acknowledgments

Although I have expressed my gratitude along the way, I also wish to publicly thank my family for their prayers and support. I also wish to thank my advisor who has given invaluable assistance throughout the research.

Those causes whose aims are worthwhile, yet have the odds against them are the causes that invigorate the mind and stir the emotions of men and women to put forth extra effort to make them happen. So it is with this topic of thesis research. When the idea was presented to use the RMC to image neutrons, it was said to be a crazy idea. The rationale for such a negative claim has solid founding in theory. The RMC would need to have thick masks to stop the fast neutrons, which would reduce the feasibility of using an RMC at all. Yet, looking at the theory from a different perspective leaves room for a possibility of success, even if remote. The masks do not need to be thick enough to stop the neutrons; rather, the masks merely need to deflect the neutrons from reaching the detector. It is that possibility of success that drove the many hours of research and several unsuccessful attempts before the research began showing encouraging results.

Nathan Boyce

Table of Contents

	Page
Abstract.....	iv
Acknowledgments.....	v
Table of Contents.....	vi
List of Figures.....	ix
List of Tables.....	xiv
List of Abbreviations.....	xv
I. Introduction.....	1
1.1 Motivation.....	1
1.2 Previous Work.....	1
1.3 Contributions of this Research.....	2
1.4 Overview of Thesis.....	3
II. RMC Theory for Neutrons.....	5
2.1 Chapter Overview.....	5
2.2 RMC Imaging Fundamentals.....	5
2.3 Neutron Sources.....	13
2.4 Neutron Interactions with Matter.....	15
2.5 Neutron Attenuation.....	16
2.6 Attenuation Masks.....	17
2.7 Neutron Detection.....	19
2.8 Simulation (Monte Carlo vs. Transport Equations).....	27
2.10 Summary.....	28
III. Experimental Procedures.....	29
3.1 Chapter Overview.....	29

	Page
3.2 RMC Operating Procedures	29
3.3 Mask Designs	36
3.4 Neutron Source Details.....	37
3.5 Simulation of RMC in MCNP.....	38
3.6 Experimental Procedures Chapter Summary.....	39
IV. Results and Analysis.....	41
4.1 Chapter Overview.....	41
4.2 Mask Feasibility Simulation.....	41
4.3 Mask experiment	44
4.4 Simulation of RMC Performance.....	45
4.5 RMC Setup with BF ₃ Detector and Cadmium Masks	46
4.6 RMC Setup with ³ He detector and cadmium masks	49
4.7 RMC Setup with ³ He detector and Borated-Epoxy masks	51
4.8 Distribution of Resampled Images	52
4.9 Energy Distribution as Source of Uncertainty.....	53
4.10 Summary.....	62
V. Conclusions and Recommendations	64
5.1 Chapter Overview.....	64
5.2 Conclusions of Research	64
5.3 Significance of Research	65
5.4 Recommendations for Future Research.....	65
5.5 Summary.....	67
Appendix A.....	68
A.1 Liquid Scintillator Detector	68
A.2 Pulse Processing	70
A.3 Pulse Shape Discrimination (PSD).....	71
A.4 Digital Equipment.....	72
A.5 PSD Implementation.....	73
Appendix B	76
B.1 LabVIEW Software	76
B.2 Cross Section, MFP, Neutron Flux, and Reaction Rate Plotting.....	76

	Page
Appendix C	80
C.1 Electronic Settings for Thermal Neutron Energy Window	80
Appendix D.....	83
Bibliography	84

List of Figures

Figure	Page
1. Figure 1: RMC Operation. Read the diagram from left to right. Although the source emits radiation isotropically, this figure only illustrates the radiation that is in the direction of the detector. The centerline of the RMC is used as the origin for image reconstruction. The masks are aligned and rotate together to selectively block the radiation from reaching the detector. The detector outputs a signal that is processed to generate a unique modulation profile for each source location. The modulation profile is then used in a reconstruction algorithm that uses knowledge of the RMC system to reconstruct the source location.....	6
2. Figure 2: Coordinate System for RMC. The origin of the coordinate systems is the point where the centerline of the RMC intersects the rear side of the rear mask. Figure from Kowash [3]......	8
3. Figure 3: Ideal Modulation Profile. The ideal modulation profile shown here is for identical masks and repeats after 180 degrees. The modulation ranges from 50% transmitted (open) to 0% transmitted (closed). A realistic measured modulation profile would be a number of transmitted particles, per mask rotation angle, measured by the detector and would include stochastic noise.....	9
4. Figure 4: Image Reconstruction Parameters. The frequency and phase components of the modulation profile give the radial and theta components of the source location in the image reconstruction.....	10
5. Figure 5: Pu-Be Neutron Energy Spectrum. The neutron energies are distributed between thermal and 10 MeV with average neutron energy of 4.6 MeV [9]. The probability that a neutron is emitted below 0.5 eV is 0.038 [12]......	14
6. Figure 6: Cross Section Data. The microscopic cross sections for ^{10}B , ^3He and natural Cd are plotted. Both ^{10}B and ^3He have their cross sections decrease in a manner that is proportional to their energies until close to 1 MeV. Natural cadmium drops much more abruptly and then exhibits some resonance behavior. Cross section data came from the KAERI website [11].	15
7. Figure 7: Fraction Transmitted for 0.08cm Cadmium. The fraction transmitted was calculated at each energy for the mask thickness using equation (1.3). Note the 50% cutoff is around 0.5 eV. Below 0.5 eV almost nothing passes through the thin layer of cadmium. However, above the cadmium cutoff energy almost everything passes directly through the material.....	18

8. Figure 8: Fraction Transmitted for 1.27 cm Borated Epoxy. The fraction transmitted was calculated at each energy for the thickness of the mask using equation (1.3). Note that the fraction transmitted does not drop as low as it does for cadmium, but it also attenuates more at higher energies. It exhibits some resonance behavior..... 19
9. Figure 9: Pulse height spectrum for BF_3 gas proportional counter. The pulse height spectrum arises from neutron absorption. It is not a direct measure of incident neutron energy, so it is not an energy spectrum. The deposited energy corresponds with the reaction products that were then detected within the active detector volume. The *wall effect* continuum arises because all or part of the energy from either reaction product may leave the detector without depositing any energy in the detector. 22
10. Figure 10: Calculated MFP for ^{10}B Based Detectors. This plot of the calculated MFP over energy shows that the MFP can be large for the detector material and would imply that very few high energy interactions occur for detectors that are a couple of cm thick..... 23
11. Figure 11: Calculated Efficiency for BF_3 detector. The efficiency was calculated using equation (1.7) over a range of neutron energies. The detection efficiency is very high for thermal and epithermal neutrons but begins to approach zero at 1 MeV and above. For this reason the detector is said to be essentially insensitive to fast neutrons..... 24
12. Figure 12: Pulse Height Spectrum for ^3He Detector. The energy deposited from an assumed monoenergetic neutron source at energy (E_n) varies based on the reaction. A full energy peak is at the incoming energy plus the Q-value of the reaction, but it may also have a wall effect. The recoil distribution ranges from near zero to its maximum value of 75% of E_n . The epithermal peak and associated wall effect arises from the neutrons that were thermalized in the environment before reaching the detector..... 26
13. Figure 13: General RMC Setup. This figure shows the RMC setup from the perspective behind the detector looking toward the source. The detectors cannot be seen because they are wrapped in cadmium. Also unseen are the masks, but they are inside the aluminum cylinder that has the motor mounted to it. The source is placed 250 cm from the detector and is mounted on a stand that moves in two directions..... 30

14. Figure 14: RMC Configured with Combined Detectors. On the left: The detectors were placed sideways to avoid the potential loss of efficiency due to the guard rings. On the right: The detectors were lined up and wrapped in cadmium. They were covered in cadmium, except for an unseen hole behind the masks, to reduce the background thermal neutron counts. 31
15. Figure 15: Motorized Mount with Source Holder. The mount holds the source securely while moving it to precise locations in the motion plane defined by the movement of the two motors. The mount is positioned so that the plane in which it can move the source is perpendicular to the centerline of the RMC. 33
16. Figure 16: Masks in RMC. The mask pattern is shown in the RMC. The mask shown is made of natural cadmium and has 4 mm slits and 4 mm slats..... 37
17. Figure 17: Pu-Be Neutron Source in Mount. The source is a 72.7 mCi Pu-Be source. The sealed source is the metallic cylinder at the end of the plastic rod that is clamped to the support stand. 38
18. Figure 18: Normalized Modulation Profiles. The surface current tally (MCNP5-F1) was used as the result for a series of simulations that measured the number of neutrons that passed through the masks at each rotation angle. 42
19. Figure 19: MCNP Generate Modulation Profile for Cadmium. The source is monoenergetic 0.025 eV neutrons and the mask is 0.08 cm thick. The modulation profile shows that the modulation is very good and close to ideal. 44
20. Figure 20: Simulated RMC Performance. Simulated results for a point source at $(15 \pm 0.5 \text{cm}, 15 \pm 0.5 \text{cm})$. Top: The simulated modulation profile illustrates the ideal modulation profile without stochastic noise with an overlay of the statistically varying modulation profile. Bottom: The simulated reconstructed image came out at $(15 \pm 1 \text{cm}, 15 \pm 1 \text{cm})$ and had an ambiguity at $(-15 \pm 1 \text{cm}, -15 \pm 1 \text{cm})$ 46
21. Figure 21: Measured BF_3 Modulation Profile and Image Reconstruction. The measured results for a 3 hour run with the known source position at $(10 \pm 0.5 \text{cm}, 0 \pm 0.5 \text{cm})$. Top: The modulation profile showing the number of detected counts for each rotation angle of the masks. Bottom: The reconstructed image obtained by running the MLEM algorithm on the measured modulation profile. The reconstructed source location was $(10 \pm 6 \text{cm}, -1 \pm 6 \text{cm})$ 48

22. Figure 22: Measured ^3He Modulation Profile and Image Reconstruction. The measured data from a three hour run with the source at known location (15 ± 0.5 cm, 15 ± 0.5 cm). Top: The measured modulation profile showing the low modulation in the signal. Bottom: The reconstructed image showing the reconstructed source location at (13 ± 6 cm, 12 ± 6 cm). 50
23. Figure 23: ^3He with Borated-Epoxy Masks. The known source position was (10 ± 0.5 cm, 0 ± 0.5 cm). Top: The recorded modulation profile for a three hour measurement. Bottom: The reconstructed image was located at (12 ± 5 cm, 4 ± 4 cm). 51
24. Figure 24: Resampled Reconstructed Locations. This plot illustrates the number of occurrences for the locations of the resampled point source image reconstructions. Three main features are present: 1) the maximum peak is almost exact for the known location of the source, 2) the peaks just above and below the maximum peak appear to have the radial component correct, but were slightly off on the angular component in the reconstructed location, and 3) the other peaks seem to appear in a ring around the maximum peak value in such a way that may indicate a implication with the algorithm. 53
25. Figure 25: Downscatter in 0.08 cm Natural Cadmium. The multi-energetic neutron source simulation from MCNP is used for this plot. The energy is values are shown per energy bin. The noticeable feature of this plot is that there are more neutrons leaving the mask at lower energies. The source of these neutrons is not very noticeable in this plot. There is a slight dip in the faster neutrons that is on a log scale so it is a lot more than it seems and the lower energy neutrons are coming out in greater numbers. 56
26. Figure 26: Zoomed in on Fast Neutron Downscatter in 0.08 cm Natural Cadmium. The number of neutrons leaving the masks is lower than the number that is incident upon the masks. The decrease in counts is desired in a mask, but the decrease in the faster region causes the increase in the thermal region, where the detector is more efficient, that was shown in Figure 25. 57
27. Figure 27: The Change in Flux with a Cd-BoratedEpoxy-Cd Sandwich Mask. The borated epoxy layer was 1.27 cm thick and had 0.08 cm cadmium layers on each side. The thermal components of the flux increased. 58

28. Figure 28: Reaction Rate Calculation Terms and Value. Top: Although the probability of interaction in the detector decreases by several orders of magnitude as the energy increases, the flux increases by several orders of magnitude over the same energy increase. Bottom: The reaction rate shown in normalized per source particle because the MCNP tally result is per source particle. 60
29. Figure 29: Decay Components for PSD. Alpha particles are the heaviest particles shown and the pulses that correspond to alpha particles have the longest decay components. Pulses that arise from gamma ray interactions have the shortest decay time. The heavier particles have a longer decay time for the same light output than the lighter particles [8]..... 69
30. Figure 30: Illustration of Digitized Pulse from NI-6111. The sampling rate for the card was 5MS/s, so one sample every 200 ns. The pulse information is not well sampled. The peak of measurement was not stable so could alter in energy and the decay time was too fast to determine accurately where a specified percentage below the peak was located. This prevented obtaining accurate information for PSD..... 74
31. Figure 31: Instrumentation Diagram for PSD with NI-6111. The detector signal goes to a preamplifier and then the signal gets split into two lines. The top line sends a pulse whose height is the decay time of the pulse into the analog input channel 0. The bottom line sends a pulse into the analog input channel 1 where the height of the pulse corresponds to the energy of the detector. The two signals are then processed in LabVIEW to perform PSD..... 75

List of Tables

Table	Page
1. Table 1: RMC Component and Desired Function. The RMC components of mask, detector, signal processing, and image reconstruction are listed with their desired functionality. The performance of the RMC is dependent upon how well the components perform the desired function.....	7
2. Table 2: Comparison of Total Normalized Reaction Rate for Mask Designs. The difference between no mask and the specific mask reflects the difference open and closed regions of the masks. Cadmium masks were the only masks that showed a decrease in the total reaction rate from no masks, whereas the others increased. As long as there is a difference, the MLEM reconstruction algorithm should still be able to reconstruct the image location.	62
3. Table 3: Settings for BF ₃ Analog Setup. The settings for each module are displayed in this table. The signal goes from the preamplifier to the amplifier to the PSA/T-SCA and then into the counter to be sent to LabVIEW.....	81
4. Table 4: Settings for ³ He Energy Window. The ³ He detector settings are different for than the BF ₃ because of the lower energy values associated with the reaction.....	82

List of Abbreviations

ADC – Analog-to-Digital Converter

BF₃ – Boron-Trifluoride (detector)

BLR – Base Line Restoration

DPP – Digital Pulse Processing

DSP – Digital Signal Processing

³He – Helium-3 (detector)

KAERI – Korea Atomic Energy Research Institute

MCNP – Monte Carlo n-Particle

MFP – Mean Free Path

MLEM – Maximum Likelihood Estimation Maximization

NIM – Nuclear Instrument Module

NSECT – Neutron Stimulated Emission Computed Tomography

Pu-Be – Plutonium Beryllium radiation source

PSD – Pulse Shape Discrimination

RHESSI – Reuven Ramaty High-Energy Solar Spectroscopic Imager

RMC – Rotationally Modulated Collimator

VI – Virtual Instrument (National Instruments LabVIEW software module)

THERMAL NEUTRON POINT SOURCE IMAGING WITH A ROTATING MODULATION COLLIMATOR (RMC)

I. Introduction

1.1 Motivation

The Department of Homeland Security needs detectors that can detect and locate nuclear devices. The Rotating Modulation Collimator (RMC) is a simple, robust imaging system whose low cost makes it a reasonable selection in an ubiquitous detector network for locating, and potentially tracking, nuclear material and/or devices wherever they may be located. Nuclear material produces both gamma ray and neutron signatures. Most of the current imaging systems focus on only one type of radiation, but the RMC is fundamentally capable of using both radiation signatures to locate the nuclear material/device with a greater confidence level. The RMC has demonstrated exceptional performance for gamma ray radiation sources but was previously untested with neutron radiation sources. The goal of this research is to demonstrate that it is possible to use the RMC to image neutron sources. The scope of the research was limited to the low energy thermal neutrons as the first demonstration test. Successful completion of thermal neutron imaging tests would advance the research toward more realistic applications.

1.2 Previous Work

The purpose of the RMC is to image radiation sources. The RMC imaging concept for x-ray and gamma ray radiation sources has been around since the 1960s when

it was proposed by Oda and Mertz [1], [2]. The primary reason for using an RMC imaging system is that it can turn the currently used, non-position-sensitive detectors into a high performance imaging system without a significant cost. Most imaging systems rely on expensive, sophisticated position-sensitive detectors. The RMC does not require a costly position sensitive detector, but operates with a single non-position sensitive detector to achieve very good spatial resolution [3]. The downside of the RMC imaging system is that traditional designs use on average only 25% of the incident radiation resulting in substantial loss in source position information.

Applications of the RMC methodology have been used in astronomy and in medical imaging. The most successful recent application of a RMC imaging system is the RHESSI system on a satellite. RHESSI uses nine RMCs in combination to image solar phenomena [4]. Sharma proposed the use of two RMCs in combination to locate greater quantities of trace elements that correspond to early stages of cancer in a process called Neutron Stimulated Emission Computed Tomography (NSECT): Detect the gamma rays that are emitted from the trace elements as they are stimulated by inelastic scattering of fast neutrons [5]. Kowash proposed to use the RMC to passively locate orphan sources using the gamma rays emitted by the radioactive sources [3]. With the desirable performance characteristics of RMCs, it is attractive to determine if it is feasible to locate and image neutron sources with the use of an RMC.

1.3 Contributions of this Research

The contributions of this work include: 1) introduction of results obtained from utilizing the RMC imaging system for neutron sources, 2) recognition of downscatter and

stream through as challenges in imaging neutron sources that have a continuous spectrum of energies with a fast neutron component, and 3) preparation for future research in pulse shape discrimination (PSD) and digital pulse processing (DPP) at AFIT. Some potential research topics for the future are: fast neutron imaging, DPP for recording an energy spectrum to use in image reconstruction, and developing a comprehensive configuration for the RMC to image both neutron and gamma ray radiation sources.

The scope and limitations of the research were aimed at experimental demonstration of feasibility for neutron point-source imaging with the RMC. The scope of the project was to focus on modification of only the detector and mask parameters for low energy neutrons. It was limited by the time available (approximately six months) and by the available radioisotopes at AFIT. To help reduce the amount of time necessary for this project, the image reconstruction algorithm was not modified from the code developed by Kowash [3]. Neutron transport equations were not developed to avoid having the project turn into a computational thesis of calculating the neutron transport through the masks. The aim of the research has been met within scope and limitations.

1.4 Overview of Thesis

The thesis describes the use of an RMC imaging system to generate images of neutron point sources and the underlying theory and experiments that lead to those results. The thesis is divided into five chapters. The first chapter introduces the research and motivation for developing the RMCs capability to image neutron sources. The chapter also provides a summary of the key contributions made by the research efforts. The second chapter of the thesis is the theory that supports the research methods. It also

describes the principles of the equipment used to complete the research. Chapter III describes the experimental methods used. Chapter IV presents the results and analysis and the specifics of the experimental procedures. The fifth and final chapter presents the conclusions of the work and provides suggestions for further research. Two appendices provide supplemental details of the research: Progress on work with a loaded liquid scintillator for neutron spectroscopy and the initial work on digitizing and processing the analog signal in the automation and control software. Also included are some of the Matlab codes used for various computations and plots.

II. RMC Theory for Neutrons

2.1 Chapter Overview

This chapter describes the theory used to develop the first neutron RMC. The fundamental concept of reconstructing an image from the measured data of the RMC imaging system is described along with which components of the RMC need to be modified to image neutron sources. The various mechanisms that neutrons interact with matter are important because the interactions influence the design of the masks and the selection of a neutron detector. The theory used to the development of the capability of RMCs to image thermal neutron point sources is described in this chapter.

2.2 RMC Imaging Fundamentals

The RMC imaging system uses a single non-position-sensitive detector with a set of patterned, rotating masks that selectively change the intensity of the incoming radiation to record, over time, a unique modulation profile that can be used to reconstruct an image of radiological sources within the angular field-of-view of the RMC. An overview of the system is shown in Figure 1. The RMC is an indirect imaging method because it uses non-image data and a system mapping function to reconstruct the source location instead of measuring the image directly. Although the RMC is an indirect imaging method, the performance characteristics, demonstrated with gamma ray and x-rays, are very desirable: In theory, the resolution can be down to the diffraction limit of the radiation type. The RMC imaging system is relatively simple compared to most

systems used for radiation imaging. The RMC imaging system is a cost effective, high resolution method to generate images of radiological sources.

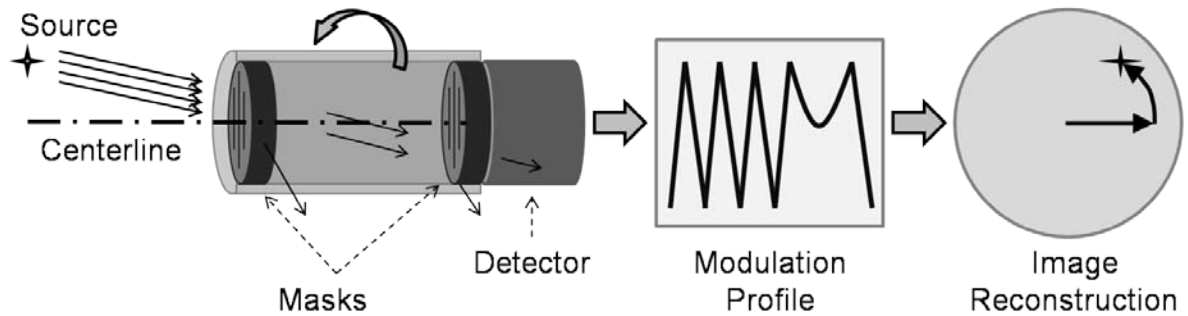


Figure 1: RMC Operation. Read the diagram from left to right. Although the source emits radiation isotropically, this figure only illustrates the radiation that is in the direction of the detector. The centerline of the RMC is used as the origin for image reconstruction. The masks are aligned and rotate together to selectively block the radiation from reaching the detector. The detector outputs a signal that is processed to generate a unique modulation profile for each source location. The modulation profile is then used in a reconstruction algorithm that uses knowledge of the RMC system to reconstruct the source location.

2.2.1 Main Components.

The RMC imaging system can be divided into four main components. The components and their desired function are listed in Table 1. The moderating material, or mask, changes the intensity of the radiation that reaches the detector. The detector measures the radiation that passes through the mask pattern. Another component generates a modulation profile from the measured radiation and mask rotation position. The image reconstruction component uses the measured modulation profile and knowledge of the RMC system to generate an image showing the source location.

Table 1: RMC Component and Desired Function. The RMC components of mask, detector, signal processing, and image reconstruction are listed with their desired functionality. The performance of the RMC is dependent upon how well the components perform the desired function.

Component	Desired Function
Masks	Either stop or deflect the incident radiation to prevent it from reaching the detector when radiation hits the mask.
Detector	Measure radiation in a way that enables discrimination of radiation type and energy
Generation of Modulation Profile	Convert the signal from the detector into a modulation profile of desired radiation type and energy range
Image Reconstruction	Reconstruct the source location using the modulation profile and a knowledge of the RMC system

2.2.2 Influence of Radiation Type on the Selection of Components.

The selection of the RMC components is influenced by radiation type of the desired imaging capability. The detector and masks are the main components whose selections are determined by the type of radiation. Selecting one material to function as a mask for all radiation types does not work. For example, the lead masks that stop gamma rays very well do very little to attenuate neutrons. The selection of mask material is based on the radiation type to ensure the mask effectively blocks that type of radiation. The detector needs to be able to measure the source radiation. The generation of a modulation profile and the image reconstruction are not influenced much by the radiation type.

2.2.3 Coordinate System Definition.

The coordinate system of the imaging system and other terminology for the RMC are defined in this section. The coordinate system, shown in Figure 2, illustrates both Cartesian coordinates and cylindrical coordinates for the RMC. The centerline of the RMC is important for both coordinate systems used in image reconstruction and is the axis about which the masks rotate, as shown in Figure 1. The field-of-view of the RMC is the range of angles that the masks create useable modulation profiles from which to reconstruct accurate images. The coordinate system is important in understanding where the source is located. Note, in this research the source location is described in the Cartesian (x,y,z) system, where the z is a fixed value.

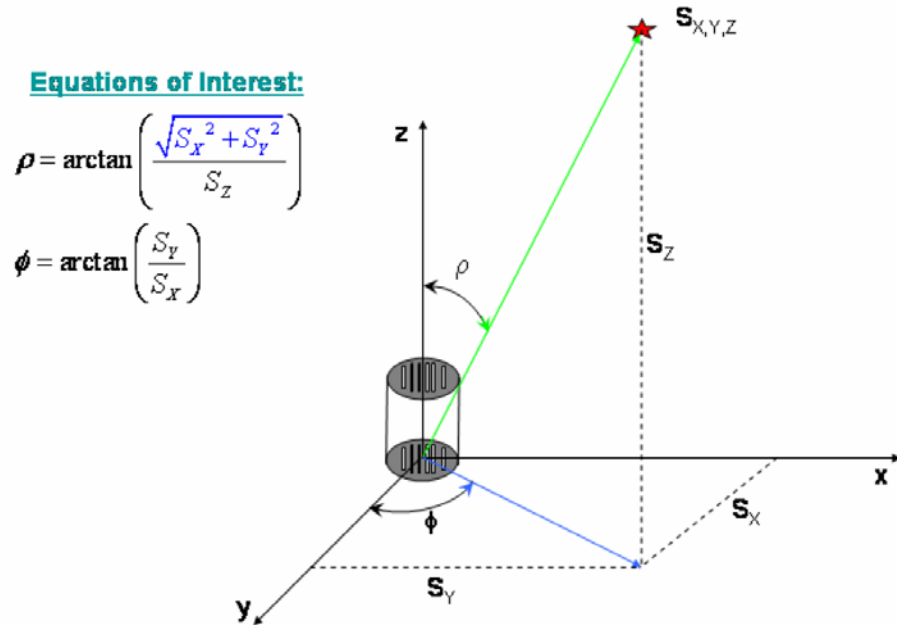


Figure 2: Coordinate System for RMC. The origin of the coordinate systems is the point where the centerline of the RMC intersects the rear side of the rear mask. Figure from Kowash [3].

2.2.4 Unique Modulation Profile.

The modulation profile is a measure of the radiation that was transmitted through the masks and detected at each mask rotation angle. An ideal modulation profile without any stochastic noise is shown in Figure 3 as a fraction of the incident radiation for half of a revolution. For symmetric masks with slits and slats of equal spacing, the modulation profile ranges from 50% transmitted (open) to 0% transmitted (closed). For identical front and back masks the unique pattern repeats itself after 180 degrees. Kowash proposed using non-identical front and back masks to produce a unique modulation pattern through 360 degrees [3].

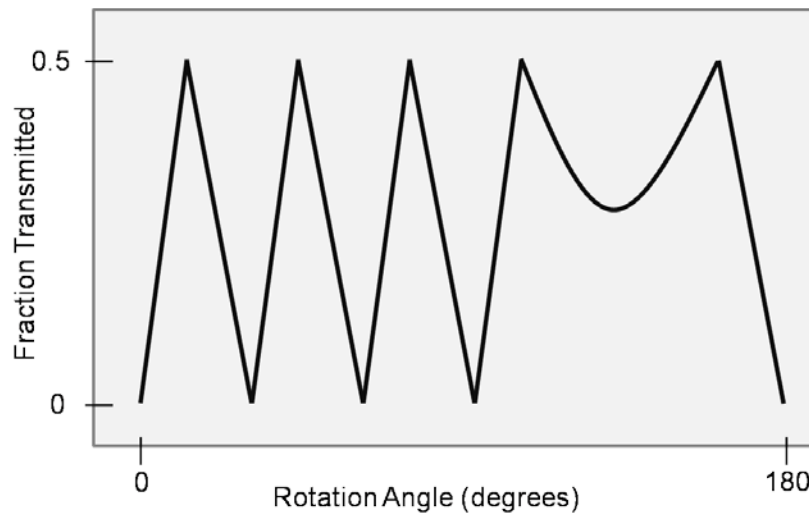


Figure 3: Ideal Modulation Profile. The ideal modulation profile shown here is for identical masks and repeats after 180 degrees. The modulation ranges from 50% transmitted (open) to 0% transmitted (closed). A realistic measured modulation profile would be a number of transmitted particles, per mask rotation angle, measured by the detector and would include stochastic noise.

The modulation profile uniquely identifies the source location by two main features. The frequency of the saw-tooth pattern in the modulation profile contains information about the radial component of the source location. The farther away the source is from the RMC centerline, the greater the frequency of the saw-tooth pattern in the modulation profile. The phase, or broad dip in the modulation profile, contains information about the theta component of the source in the image reconstruction. Figure 4 illustrates the principles of the image reconstruction overlaid on top of a simulated reconstructed image. In this research, an image reconstruction algorithm is used to generate source images.

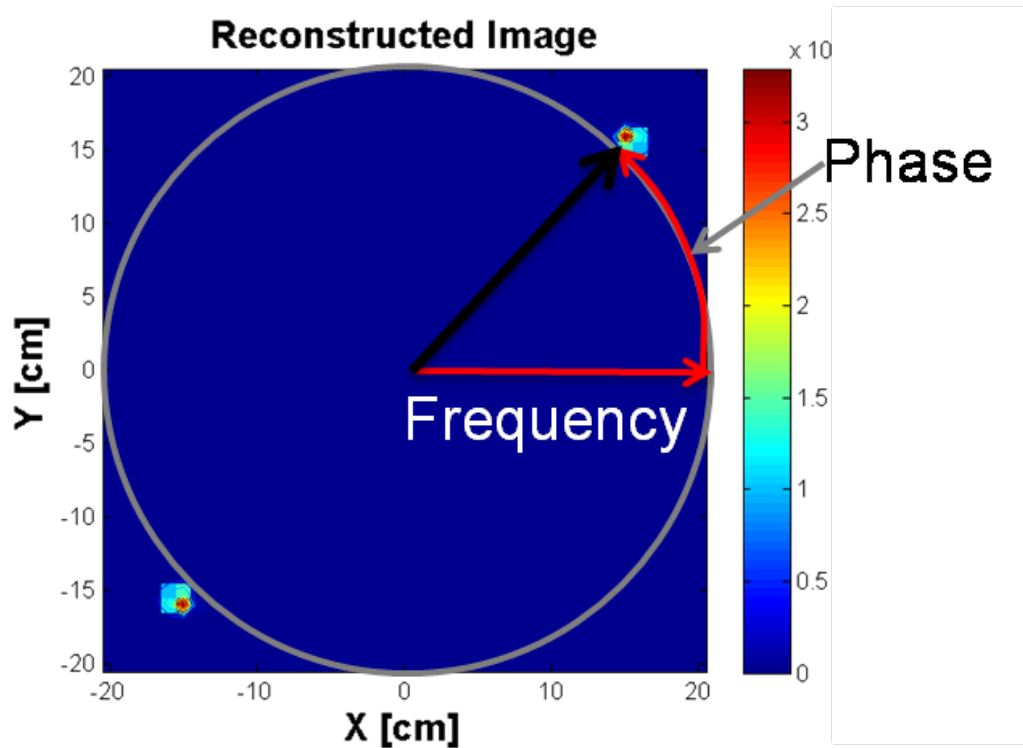


Figure 4: Image Reconstruction Parameters. The frequency and phase components of the modulation profile give the radial and theta components of the source location in the image reconstruction.

2.2.5 Image Reconstruction Algorithm.

Indirect imaging methods require an image reconstruction algorithm to create an image from raw data. The image reconstruction algorithm can use a deterministic or a statistical method. In this research a statistical image reconstruction algorithm using the principle of maximum likelihood is used to generate an image from the modulation profile. The algorithm used is the *Maximum-Likelihood-Expectation-Maximization* (MLEM) algorithm developed by Kowash for RMC image reconstruction [3]. The MLEM algorithm uses an iterative technique that alternates between expectation and maximization steps [6]. Because it maximizes the likelihood for a Poisson data model, the MLEM is well-suited for high-noise, low-count environments [6],[7].

The iterative process of the MLEM is traditionally given as

$$\lambda_j^{n+1} = \frac{\lambda_j^n}{\sum_i a_{ij}} \sum_i a_{ij} \left(\frac{y_i}{\sum_k \lambda_k^n a_{ik} + b_i} \right), \quad (1.1)$$

where λ is the Maximum-Likelihood Estimation (MLE), and a_{ij} is a system matrix that contains the probabilities that a particle emitted from the source pixel (j) is detected when the masks are in the rotational position (i), y is the measured data, and b is the background [3].

When maximizing the likelihood, it is important to use an accurate model of the physics. Kowash developed a model for determining the expected number of measured counts in the n^{th} time bin for a Poisson process and can be written as

$$y_n = \text{Poisson} \left\{ \tau_n \left[\alpha \cdot \varepsilon(E) \cdot \frac{\Omega(\rho, \phi, z)}{4\pi} \cdot [P_n(\rho, \phi, z) + P_n^C(\rho, \phi, z) \cdot \lambda(E)] + b(E) \right] \right\}, \quad (1.2)$$

where τ_n is the dwell time, α is the source activity in Becquerel [Bq], P_n is the probability that a particle emitted isotropically from a location ρ, ϕ, z (given in cylindrical coordinates) and incident on the RMC masks will pass through an open slit in the masks and hit the detector, ε is the energy dependent detector efficiency, $\Omega/4\pi$ is the solid angle subtended by the front mask of the RMC from the source, and $b(E)$ is the energy dependent background rate in counts per second (cps). The complement of the mask transmission probability P_n^C , multiplied by an energy dependent attenuation factor is the probability that a photon incident on the RMC masks is incident on a blocked element but passes through to the detector [3].

In the algorithm developed by Kowash, there are some important variables that can be adjusted to more accurately model the actual RMC parameters. These variables will be referred to as the *fidelity variables* because they directly relate to the fidelity of the model. The fidelity variables relate to the mask design properties, the detector properties, and system operation. In an experimental image reconstruction the fidelity variables are set at values that correspond to the experimental setup. The specific parameters of the RMC configuration determine the values of the fidelity variables used in the image reconstruction algorithm.

2.2.6 Uncertainty in Reconstruct Image.

The uncertainty in the reconstructed source location is found by using a *Bootstrap* re-sampling technique, which is based on the statistical concept of multiple independent observations or measurements. Each count and every revolution of the RMC can be

considered an independent measurement. A modulation profile is generated for every revolution, even if it is not well defined. A large number (50-1000) independent modulation profiles are recorded and summed together to produce the modulation profile used in the image reconstruction. Another modulation profile is generated from the same set of independent observations by randomly re-sampling (with replacement) for each point in the modulation profile. The new modulation profile is slightly different than the original and is used to reconstruct another image. By generating hundreds or thousands of re-sampled modulation profiles a large number of slightly different images are reconstructed and stored. From all the reconstructed images, the mean and standard deviation is calculated to determine the uncertainty.

2.3 Neutron Sources

When validating any new imaging technique, it is important to have a fundamental understanding of possible neutron sources the RMC could image. Neutron sources are categorized by the reaction that emits the neutrons. Knoll describes the following four different sources: spontaneous fission, radioisotope (α, n) sources, photoneutron sources, and reactions from accelerated charged particles [8]. To avoid the confounding effects of multi-energetic sources, the best type of neutron source to use for proof-of-concept is one that is monoenergetic. A limitation of the research was that an ideal source could not be obtained in time for the research. The only available neutron sources were radioisotope (α, n) sources: Pu-Be sources with different activities.

An alpha-neutron (α, n) reaction is one in which an alpha particle is absorbed by a suitable target isotope that emits a neutron after the absorption. The specific (α, n) source in this research is a Pu-Be neutron source: ^{239}Pu spontaneously emits alpha particles that are absorbed in ^9Be isotope to cause a 5.71 MeV (Q-value) reaction that produces ^{13}C , which is unstable so it emits a neutron. The Pu-Be source emits neutrons in a distribution, shown in Figure 5, of energies ranging from thermal to 10 MeV with an average neutron energy of 4.6 MeV [12].

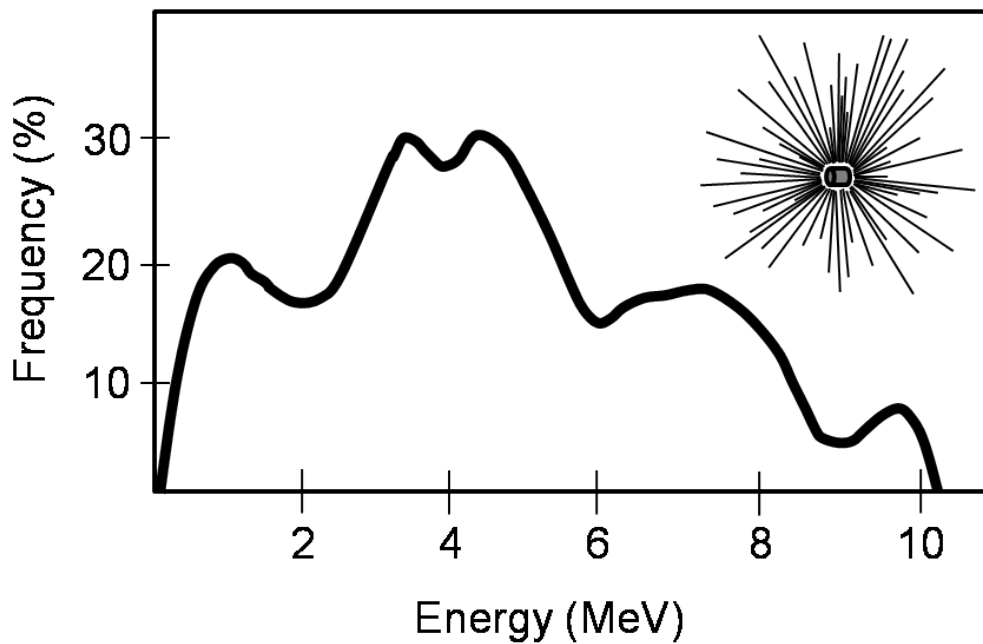


Figure 5: Pu-Be Neutron Energy Spectrum. The neutron energies are distributed between thermal and 10 MeV with average neutron energy of 4.6 MeV [9]. The probability that a neutron is emitted below 0.5 eV is 0.038 [12].

2.4 Neutron Interactions with Matter

Neutron interactions with matter are complicated because neutrons are neutral particles that do not respond to the Coulomb force. The two primary ways that a neutron interacts in matter are scattering or absorption with the nucleus of a target atom. In the scattering reaction, the neutron changes direction and loses some energy to the nucleus of the impacted atom. The microscopic cross section is the probability of a certain reaction occurring (i.e. scattering, absorption, fission). As shown in Figure 6, the microscopic cross section is an energy dependent material property. The cross sections for ^{10}B and ^3He shown follow the $1/v$ relationship, but the cadmium cross section drops off quickly. The macroscopic cross section is obtained from the microscopic cross section by multiplying it by the number density of the material.

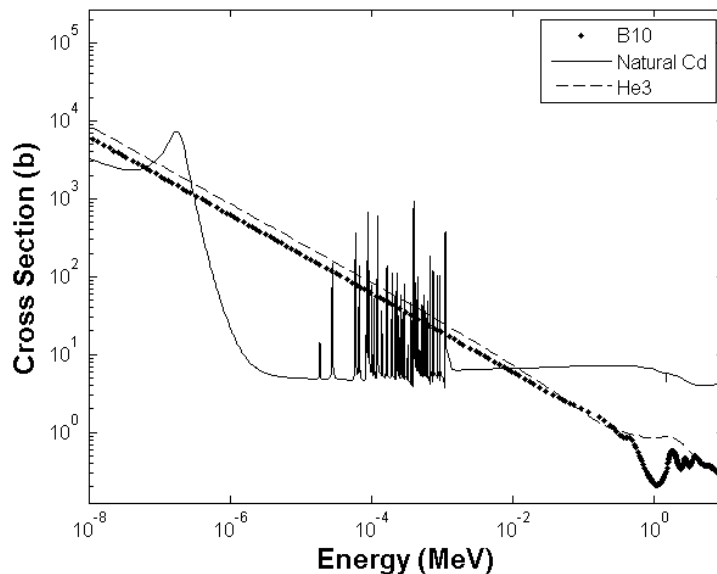


Figure 6: Cross Section Data. The microscopic cross sections for ^{10}B , ^3He and natural Cd are plotted. Both ^{10}B and ^3He have their cross sections decrease in a manner that is proportional to their energies until close to 1 MeV. Natural cadmium drops much more abruptly and then exhibits some resonance behavior. Cross section data came from the KAERI website [11].

2.5 Neutron Attenuation

Neutron attenuation is an important physical aspect that influences the design of the RMC components. The narrow-beam attenuation equation provides a conservative approximation for the fraction of neutrons transmitted by a moderating material:

$$\frac{I}{I_0} = e^{-\Sigma_{tot} x} \quad (1.3)$$

where: I is the intensity of neutrons transmitted; I_0 is the intensity of neutrons incident upon the material; Σ_{tot} is the total macroscopic cross section; and x is the thickness of the material. The total macroscopic cross section is the sum of all the macroscopic cross sections for possible interactions, e.g., scatter and capture, in the material. A limitation of equation (1.3) is that it does not account for scattered neutrons that reach the detector location, nor does it account for downscatter in multi-energetic problems. A better approach would be a neutron transport equation/computation for the specific problem. The neutron scatter is accounted for through neutron transport equations, which, due to limitations, were not implemented in this research. The principles of neutron interactions with matter and the attenuation of neutrons through materials can now be applied to the selection of mask parameters (material and thickness) and the selection of a non-position-sensitive detector.

2.6 Attenuation Masks

The purpose of the masks is to selectively change the intensity of the incoming radiation. To determine an approximation of the number of neutrons that pass through a mask, equation (1.3) was used with the macroscopic cross section of the mask material and its thickness. Figure 7 and Figure 8 show the approximation of the fraction transmitted for 0.08 cm natural cadmium masks and 1.27 cm borated-epoxy (5% natural B) masks respectively. The thin cadmium masks effectively block the low energy radiation (below 0.5 eV) from passing through the masks, yet do little to stop the higher energy neutrons. The thicker masks made of borated epoxy do not block as effectively, but have a greater energy range for neutron attenuation. The approximations for the mask attenuation indicate good modulation efficiency at low neutron energies, but would be expected to exhibit poor performance at higher energies.

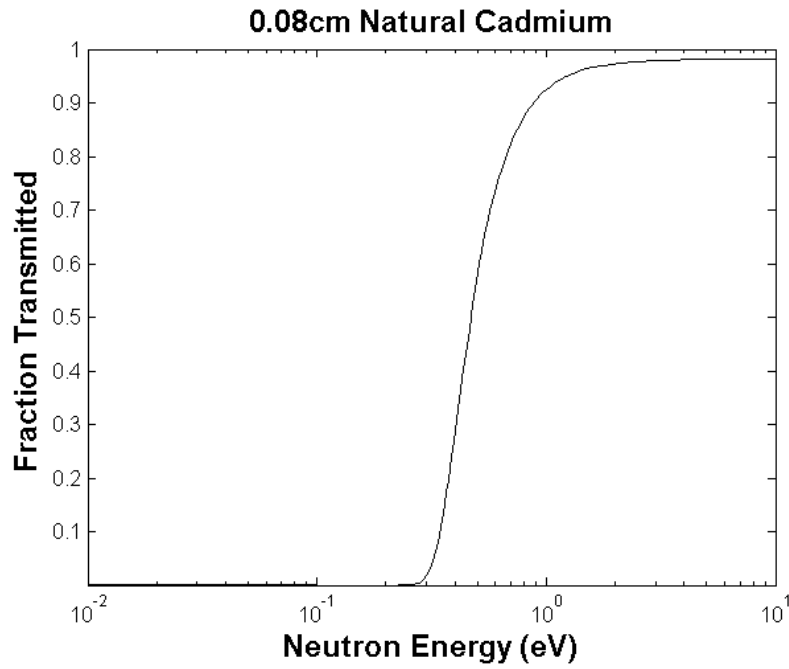


Figure 7: Fraction Transmitted for 0.08cm Cadmium. The fraction transmitted was calculated at each energy for the mask thickness using equation (1.3). Note the 50% cutoff is around 0.5 eV. Below 0.5 eV almost nothing passes through the thin layer of cadmium. However, above the cadmium cutoff energy almost everything passes directly through the material.

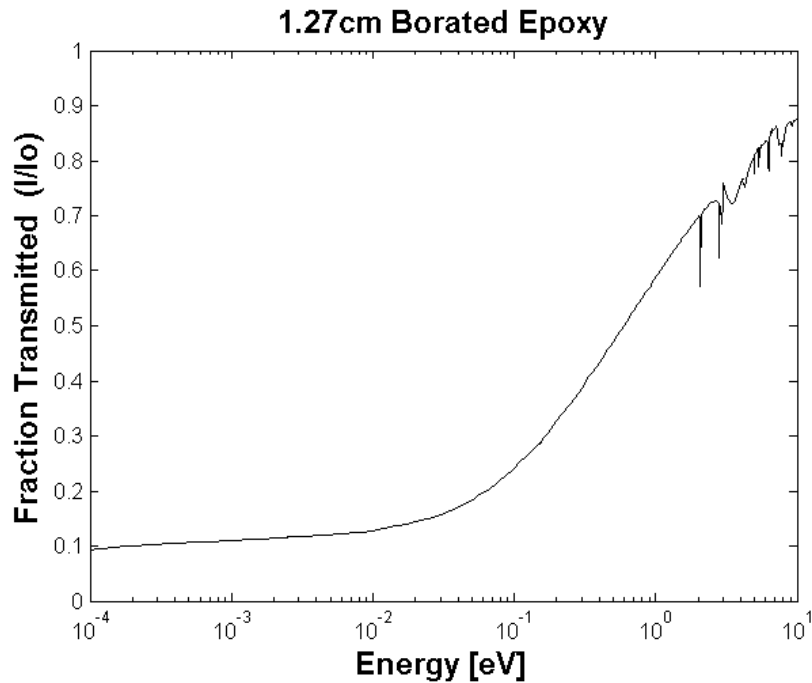


Figure 8: Fraction Transmitted for 1.27 cm Borated Epoxy. The fraction transmitted was calculated at each energy for the thickness of the mask using equation (1.3). Note that the fraction transmitted does not drop as low as it does for cadmium, but it also attenuates more at higher energies. It exhibits some resonance behavior.

2.7 Neutron Detection

Detecting neutrons is a challenging process because they are neutral particles and carry no charge with which to create a detectable signal. Neutron detection is primarily done by detecting the byproducts of a neutron induced reaction. Most byproducts of neutron-induced reactions carry a charge which creates ionizations as they slow down in the detector. These ionized particles are collected in an electric field and used to generate a voltage signal that is proportional to the energy of the initial reaction particle. The rate at which neutron induced reactions occur depends upon the cross section for the reaction

and the neutron flux in the detector. An equation for the Reaction Rate Density (R_{RX}) for a specific energy and material is

$$R_{RX} = \varphi(r) \Sigma, \quad (1.4)$$

where $\varphi(r)$ is the neutron flux, and Σ is the macroscopic cross section for the reaction of interest. A more general and comprehensive equation for the R_{RD} over all energies is

$$R_{RX} = \int_0^{\infty} \varphi(r, E) \Sigma(E) dE, \quad (1.5)$$

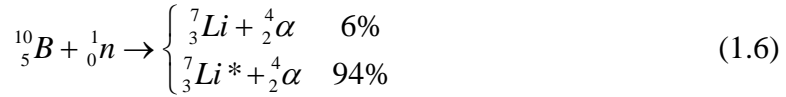
where the neutron flux and the macroscopic cross sections are energy-dependant [8]. The total reaction rate for the detector is then obtained by multiplying the active volume by the R_{RX} calculated from equation (1.5).

Although there are several detectors that can measure neutron radiation, only those used in this research will be described. Neutron capture and scatter reactions are the main reactions of interest in the detectors used for this thesis. The detectors used in this research are boron-trifluoride enriched in ^{10}B ($^{10}\text{BF}_3$) gas proportional detector and helium-3 (^3He) proportional detector because of their availability and neutron detection capability. Several other detectors can be used to detect neutrons, but an ideal detector for all neutron detection applications does not exist. The next few subsections discuss the neutron detectors that were used in the research.

2.7.1 Boron-trifluoride (BF_3) Gas Proportional Neutron Detector.

Neutrons are indirectly measured with a BF_3 gas proportional detector. The neutrons cause a $^{10}\text{B}(n, \alpha)^7\text{Li}$ reaction to occur in the detector and a signal is generated

when the ${}^7\text{Li}$ and alpha particles slow down in the detector. The neutron reaction that takes place is with boron, specifically ${}^{10}\text{B}$, and is called the ${}^{10}\text{B}(n, \alpha){}^7\text{Li}$ reaction. The reaction is described as follows



where the asterisk indicates that the Li is in an excited state, which quickly decays by emitting a gamma ray. The branching ratio indicates that 6% of the time, a neutron is absorbed in ${}^{10}\text{B}$ and, the ${}^7\text{Li}$ is produced in its ground state, while 94% of the time, it is produced in an excited state. A typical BF_3 pulse height spectrum is shown in Figure 9. The height of the detected pulse varies even for the same reaction depending upon how much of the reaction energy is deposited within the detector. The spectrum of the BF_3 detector is not directly related to the energy of the incident neutron. If the neutron is absorbed in a region where both of the byproducts are absorbed in the detector, then the pulse height value is the full energy peak of the reaction. Due to the branching of the reaction, the spectrum has two full energy peaks corresponding to the branch of the reaction that caused it. Again, the BF_3 detector output is a pulse height spectrum that does not contain any information about the energy spectrum of the incident radiation. Each pulse height that falls within the range resulted from the capture of a neutron by ${}^{10}\text{B}$ nucleus. Because of the low density of the BF_3 gas and the corresponding *mean free path* (MFP) of neutrons in the detector, it is assumed that the energy of the absorbed neutron corresponds primarily to thermal neutrons.

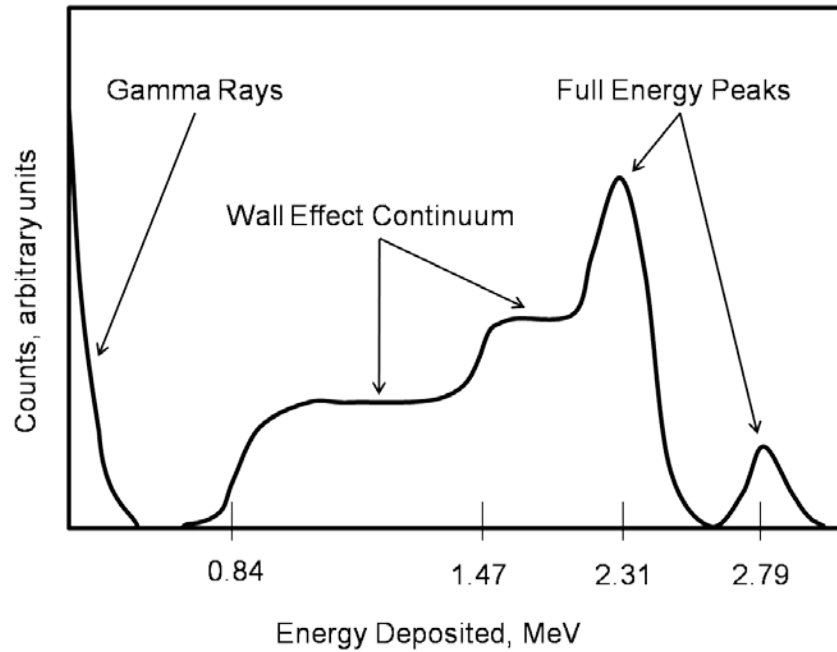


Figure 9: Pulse height spectrum for BF_3 gas proportional counter. The pulse height spectrum arises from neutron absorption. It is not a direct measure of incident neutron energy, so it is not an energy spectrum. The deposited energy corresponds with the reaction products that were then detected within the active detector volume. The *wall effect* continuum arises because all or part of the energy from either reaction product may leave the detector without depositing any energy in the detector.

Although some gamma rays are responsible for pulses, they may be removed from the signal because the energy is lower than the energy of the boron capture. The detected pulse height spectrum is often referred to as the *wall-effect* because the deposited energy changes based on whether or not a secondary reaction product escapes through the wall of the detector. The pulses that arise from a gamma ray interaction in the detector are discriminated by excluding low-amplitude pulses because the gamma rays do not deposit sufficient energy to cause a pulse of similar amplitude with a neutron pulse.

The MFP of a neutron in any material, including the material in a detector, varies by energy. The MFP in a medium is the inverse of the total macroscopic cross section. The MFP is defined as the average distance a particle will travel before interacting with the medium. Figure 10 conceptually illustrates how the MFP varies over energy for a BF_3 detector. The implication of a large MFP is that few interactions would occur in the detector of a few cm thick.

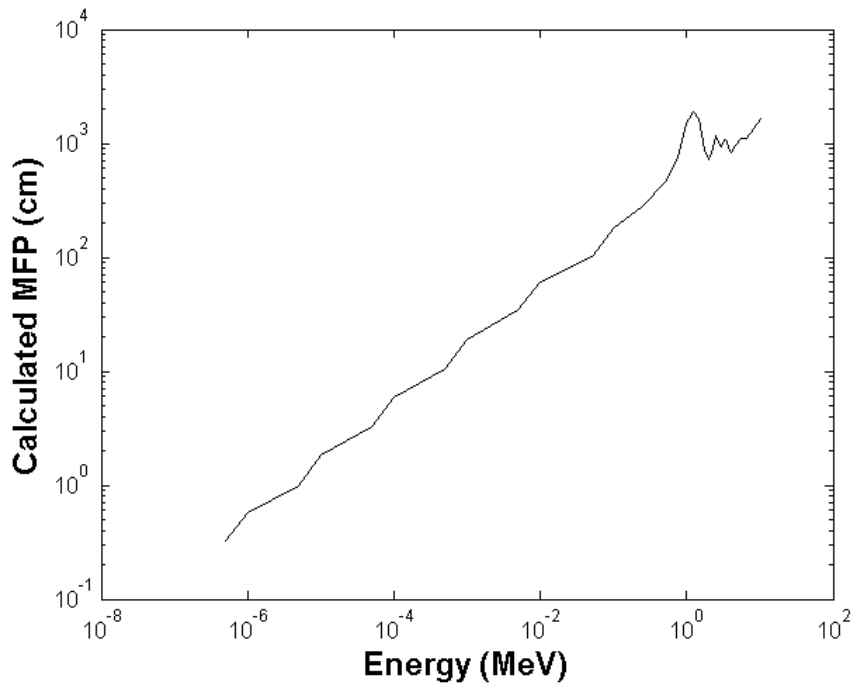


Figure 10: Calculated MFP for ^{10}B Based Detectors. This plot of the calculated MFP over energy shows that the MFP can be large for the detector material and would imply that very few high energy interactions occur for detectors that are a couple of cm thick.

The efficiency of the detector can be measured in two different methods: geometric and intrinsic. The geometric efficiency is described as the percent of the particles emitted from the source that reached the detector. The intrinsic efficiency is

determined as what percent of the radiation that entered the detector was detected. The BF_3 intrinsic efficiency is calculated for neutron energy by:

$$\varepsilon(E) = 1 - e^{-\Sigma_a(E)x} \quad (1.7)$$

where $\Sigma_a(E)$ is the macroscopic absorption cross section for ^{10}B at neutron energy E , and x is the distance in the active volume that the particle would travel [8]. Although the distance traveled in the detector varied, a constant distance of 2 cm was used to calculate the detector efficiency that is shown in Figure 11. The detection efficiency of the BF_3 is highest for thermal neutrons but begins to approach zero at 1 MeV and above. For this reason the detector is said to be essentially insensitive to fast neutrons.

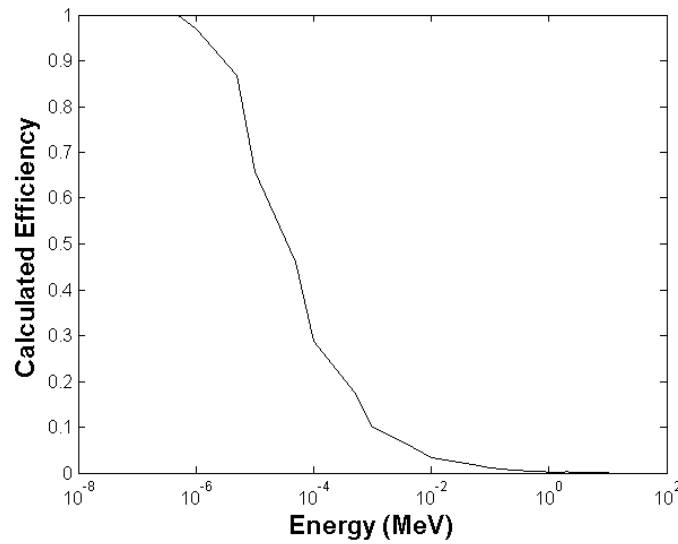


Figure 11: Calculated Efficiency for BF_3 detector. The efficiency was calculated using equation (1.7) over a range of neutron energies. The detection efficiency is very high for thermal and epithermal neutrons but begins to approach zero at 1 MeV and above. For this reason the detector is said to be essentially insensitive to fast neutrons.

2.7.3 ^3He Neutron Detector.

The ^3He detector is sensitive to a broader energy range than the BF_3 tubes. Because ^3He cannot be made into a solid compound, the ^3He detectors are constructed into sealed tubes that use the noble gas as a proportional gas detector [8]. The reaction that ^3He detectors use to detect neutrons is



with a Q-value of 764 keV. Because the range of the reaction products is sufficiently large compared to the size of the detector, some of the energy escapes out through the walls of the detector. The ^3He detector pulse height spectrum exhibits a similar wall effect as the BF_3 detector pulse height spectrum; however, the steps occur at the energies of the ^3He reaction products. The first step would correspond to 191 keV for the triton, and the second step would be at 573 keV for the proton. These lower energies for the wall effect are closer to the gamma ray energies.

Detectors using ^3He are more efficient than BF_3 detectors because they can operate at much higher pressures, which also increases fast neutron sensitivity [8]. The pulse-height tally of the ^3He detector is different in the presence of fast neutrons, as illustrated in Figure 12. The figure can be used both conceptually and quantitatively. If the detector dimensions are small compared to the ranges of the secondary particles, then the wall effect would be present in the spectrum to the left of both peaks. One of the peaks is the full-energy peak that is visible at the energy of the incident fast neutron plus

the Q-value of the reaction, which is 764 keV for the ^3He absorption reaction. Another feature on the spectrum is the presence of the recoil distribution caused by the transfer of energy to the helium nucleus from the scattering of the neutrons. The maximum value is calculated from a neutron kinematics calculation to be 75% of the energy of the incoming neutron. The epithermal peak “rides on top” of the recoil distribution and corresponds to the detection of neutrons in the thermal energy region and is the same as it would appear without the presence of faster neutrons.

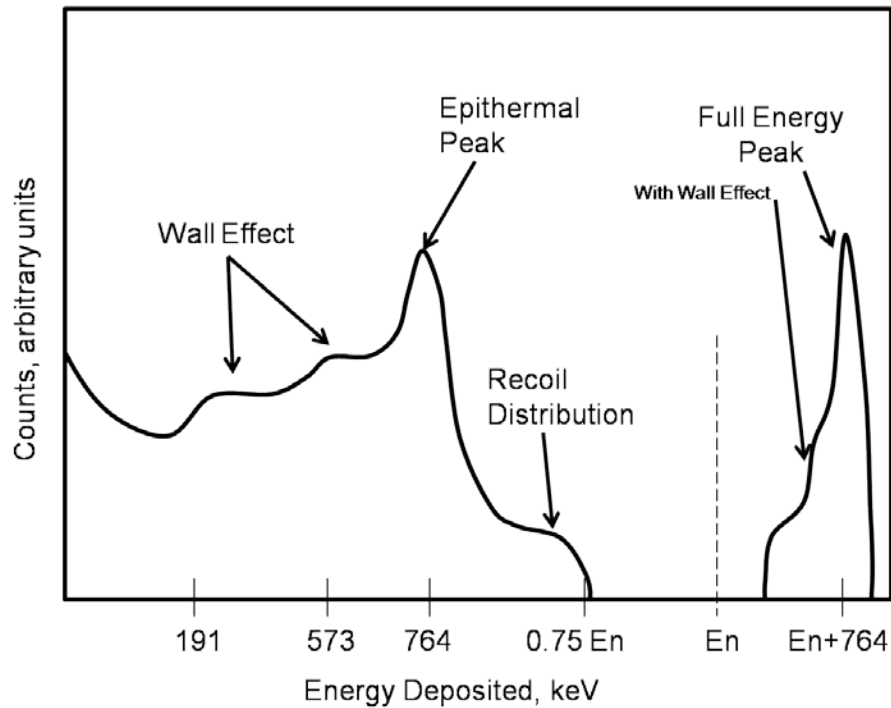


Figure 12: Pulse Height Spectrum for ^3He Detector. The energy deposited from an assumed monoenergetic neutron source at energy (E_n) varies based on the reaction. A full energy peak is at the incoming energy plus the Q-value of the reaction, but it may also have a wall effect. The recoil distribution ranges from near zero to its maximum value of 75% of E_n . The epithermal peak and associated wall effect arises from the neutrons that were thermalized in the environment before reaching the detector.

2.8 Simulation (Monte Carlo vs. Transport Equations)

Simulation is an important consideration when designing an experiment. As long as the simulation accurately reflects the actual model and the appropriate physics are included, the results of the simulations can help prevent performing experiments that are doomed from the beginning. The results are only as good as the fidelity of the model and the physics that went into the simulation. Simulation of neutron interactions in a medium can be executed through deterministic neutron transport equations or through statistical Monte Carlo computer codes. Monte Carlo methods typically use a computer to simulate, in a random manner, large quantities of particles and report a statistical answer. Due to the limited time available for the research, the choice was made to use the Monte Carlo code MCNP [13] because of its availability.

As an example of the particle tracking done in Monte Carlo, consider an isotropic point source that emits a neutron in a random direction. The distance the neutron travels in the medium is determined by taking into account all the possible reactions and the probability of each occurring, and then, using random numbers to determine which reaction will occur, and at what distance. If the reaction is a scatter reaction, then the neutron changes direction and transfers some energy to the other particle in the collision. With the new direction and energy the particle continues to be tracked in the same manner as before until the particle is absorbed or the particle energy drops below the level that the code will track. If a reaction occurs where multiple particles are formed, the code stores the newly formed particles, and continues to track the initial particle.

When the initial particle has been tracked to the end, the code sequentially returns to the next stored particle and tracks its interactions until the end [13].

2.10 Summary

This chapter contains the fundamentals of RMC imaging systems and describes the theory about how the RMC can be used to image neutron sources. The detector and masks are the main components of the RMC modified for neutron imaging capability. The masks are made of materials that have high cross-sections for neutrons to stop them from reaching the detector. The detector is able to measure the neutrons. The generation of the modulation profile is necessary to reconstruct an image. The MLEM algorithm is used as the reconstruction algorithm. The neutron source that was available for the research was the Pu-Be neutron source of poly-energetic neutrons. The two main methods of simulation (deterministic and Monte Carlo) were described. The theory chapter has described the concepts that are used in this research.

III. Experimental Procedures

3.1 Chapter Overview

This chapter describes the experimental equipment and setup in a general way that applies to several of the experiments. The operating procedures for the RMC, the mask designs, source details, and MCNP simulation are described. The details of setting up energy windows for the BF_3 and ^3He detectors are the last sections before the chapter summary. The specific experimental setups described in Chapter IV, *Results and Analysis*, are in accordance with the procedures described in this chapter.

3.2 RMC Operating Procedures

The RMC used in this research was a modified version of the prototype RMC developed by Kowash [3]. The following paragraphs describe the general operating procedures for the RMC. Operating procedures include: 1) the detector positioning and shielding, 2) the alignment and calibration of the masks, 3) the calibration of the source location, and 4) the control of the RMC. Afterward, the mask designs for both mask types used are described followed by a description of the neutron source used. The procedures are helpful in understanding the general RMC setup, which is shown in Figure 13.

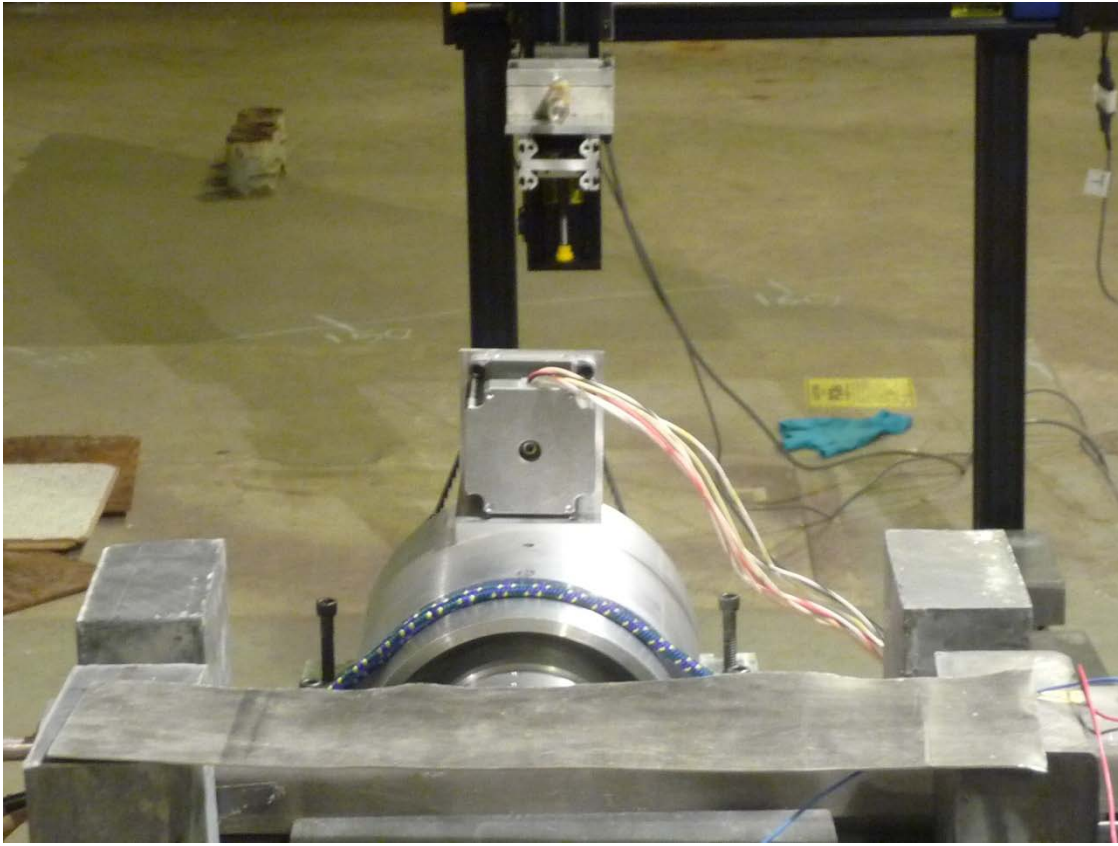


Figure 13: General RMC Setup. This figure shows the RMC setup from the perspective behind the detector looking toward the source. The detectors cannot be seen because they are wrapped in cadmium. Also unseen are the masks, but they are inside the aluminum cylinder that has the motor mounted to it. The source is placed 250 cm from the detector and is mounted on a stand that moves in two directions.

3.2.1 Detector Positioning and Shielding.

The placement of the detector in the RMC setup was carefully planned to measure the modulated signal. The BF_3 and ^3He detectors were sealed tubes of approximately 2.5 cm in diameter and 31 cm in length. The tube detectors were placed sideways, as shown in Figure 14, to avoid the potential problem of decreased efficiency that would exist if the ends of the tubes were constructed with guard rings. The RMC detector mount was

removed because it only had a 13 cm diameter and could not hold the detectors. Removing the detector mount also reduced the length of the tube and limited the range the masks could be separated. In order to fill in the full cross sectional area of the masks, five detectors (three next to the masks and two behind) were combined together.



Figure 14: RMC Configured with Combined Detectors. On the left: The detectors were placed sideways to avoid the potential loss of efficiency due to the guard rings. On the right: The detectors were lined up and wrapped in cadmium. They were covered in cadmium, except for an unseen hole behind the masks, to reduce the background thermal neutron counts.

With the detectors turned sideways, they extended beyond the area blocked by the masks and required shielding to reduce background in the non-position sensitive detector. The detectors were wrapped in a 0.08 cm thick layer of natural cadmium with an opening that lined up with the RMC masks. The purpose of the cadmium, with a high absorption cross section for thermal neutrons, is to stop most of the thermal neutrons from entering the detector. Care was taken to reduce the background counts by shielding the exterior portion of the detectors with cadmium.

3.2.2 Alignment and Calibration of Masks.

The masks were positioned inside the flight tube, aligned, and calibrated. The flight tube used was a 25 cm long cylindrical tube whose inner diameter is the same as the outer diameter of the masks. The masks fit snugly into the flight tube and were tightened with set screws. The separation distance between the masks was limited to the size of the flight tube, which size was determined by the configuration of the detector mount to no more than 22 cm. The masks were aligned using a flat calibration bar resting on corresponding slats in both the front and back masks. One of the masks was rotated until it was aligned with the calibration bar. A level, placed on the calibration bar, was used to ensure the mask slats were horizontal. The position decoder was read and calibrated to be the mask angle of zero rotation with horizontal position of the slats. The uncertainty in the angle would not be over a degree.

3.2.3 Calibration of Source Position.

In order to determine the accuracy of the reconstructed image, the true source position needed to be determined in relation to where the RMC was located. The process involved fixing the position of the RMC and calibrating the position of the mount holding the source. The motorized mount with source holder is shown in Figure 15. The movement of the source was done by moving the mount that supported the source. The movement of the mount kept the source in a plane perpendicular to the centerline of the RMC at a fixed distance along the centerline. The RMC was firmly mounted on a table using c-clamps to prevent its movement. The source was secured to the mount by a

custom clamp to hold the source in place. It was designed for quick placement: the source is able to slide in and be tightened quickly. Once the source is in place, the mount can be moved around remotely, to within a few micrometers in both directions, by moving the mount through computer commands without a person getting close to it.

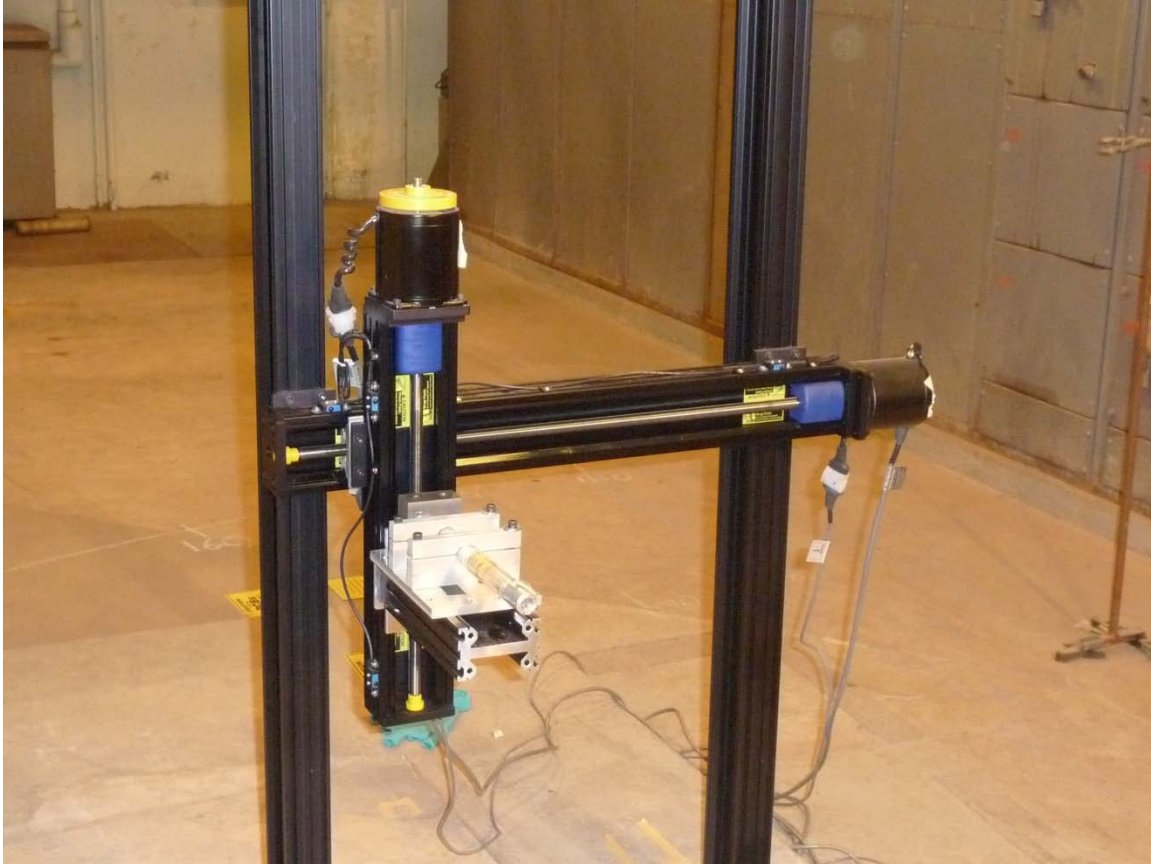


Figure 15: Motorized Mount with Source Holder. The mount holds the source securely while moving it to precise locations in the motion plane defined by the movement of the two motors. The mount is positioned so that the plane in which it can move the source is perpendicular to the centerline of the RMC.

The source position was calibrated in reference to the RMC by calibrating the mount that holds the source. The calibration process involved finding the *home position* on the mount, which is the position where the source is in line with the centerline of the

RMC, and the distance from the RMC to the home position. Because the mount can move in the horizontal and vertical directions the movement of the source can be defined as a plane. If the horizontal component of the plane is perpendicular to the RMC centerline, then the distance from the front mask of the RMC to the plane indicates the z component of the source location. The distance from the front mask to the home position was determined by the use of a laser distance finder to be 230 cm.

The *home position* was calibrated using a ^{57}Co point source of gamma rays and the components of the RMC for gamma rays. Then leaving the base of the RMC firmly fixed to the table, the RMC components were exchanged for neutron related components. The custom clamp mount on the mount was made to position the neutron source in the same place as the gamma source to reduce the effect of replacing the gamma source with the neutron source. The calibration process with the gamma source involved several image reconstructions with the source at various locations inside the FOV. Because of the accuracy of the gamma imaging RMC, the home position is determined to within 0.5 cm in both x and y directions. The challenge of finding the centerline of the RMC using the imaging device itself is that the RMC has a *blind spot* along its centerline that is caused because the modulation profile is the same at every rotation angle. To compensate for the blind spot, several image reconstructions were performed to back-track the home position. Once the home position was determined, the source was moved to the center position to verify that the modulation profile was flat over the rotation angles, like it would be in the center, or home position.

3.2.4 Control of RMC.

When controlling the RMC, it is necessary to ensure that the rotation angle and detected counts correspond to each other correctly. The prototype RMC control is currently done using a custom automation and control module. The software is a LabVIEW Virtual Instrument (VI) to control the mask rotation speed and acquire data, which it stores as the modulation profile. Rotation speed, angular position and detected counts need to be controlled or monitored. The motor rotation speed is set to 15 revolutions per minute, but actual mask rotation varied slightly. The detected counts are monitored and recorded along with the angular position for a controlled amount of time as specified in the custom VI. The angular position is monitored using an optical position decoder with resolution of 72,000 increments per revolution. The control of data acquisition needs to generate an accurate modulation profile that can be used in an image reconstruction algorithm.

3.2.5 Generation of Modulation Profile.

The generation of a modulation profile combines two processed signals together. As a reminder, the modulation profile is the number of measured radiation at each mask rotation angle. The pulse height from the detector is converted to represent energy and the second signal from the position decoder is converted to indicate the mask rotation angle. The two coincident signals are stored together in the automation and control software used to generate the modulation profile either in pseudo-real time or post processed.

3.2.6 Summary of RMC Operating Procedures.

To review, the source was placed on a mount that could be moved in known increments along a plane created by the horizontal and vertical motors. Affixed to a table, the RMC was situated in a way to have the FOV contain the mount with the source on it. The source mount was calibrated to the centerline of the RMC using a gamma ray RMC. Once calibrated, the RMC mask and detector components were switched out for the experimental components. The control of the RMC ensures proper rotation and measurement of data to accurately generate a modulation profile.

3.3 Mask Designs

Two masks sets used were constructed for the research: One of cadmium and the other of borated epoxy. The borated epoxy masks were 12.7 mm (½ inch) thick and were composed of 95% epoxy and 5% natural boron, which is 20% ^{10}B and 90% ^{11}B . The other mask set was cut from natural cadmium that was 0.8 mm ($1/32^{\text{nd}}$ of an inch) thick. The design of the masks was a series of eight evenly spaced slats, where the dimensions were 4 mm slits and 4 mm slats. The mask diameter was 76.2 mm (3 inches). Although the set of cadmium masks was actually constructed of both cadmium and aluminum, it was effectively only made of the cadmium. The thermal cross section for cadmium is over 3,000 barns, whereas for aluminum the thermal cross section is less than 10 barns. Although the aluminum still has a cross section, it is not very much compared with the cadmium. So, most of the attenuation would be done by the cadmium. The aluminum was used to hold the cadmium in place in the flight tube because the cadmium was too thin to set screw into place. The two materials were taped together using double-sided

tape. The aluminum layer was 6.3 mm (1/4 inch) thick. Both the front and back mask were constructed of both the cadmium and aluminum layers, but the cadmium was the real mask material. Figure 16 shows a cadmium mask in the RMC configuration.

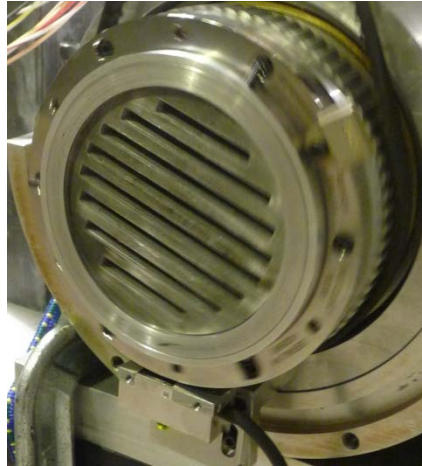


Figure 16: Masks in RMC. The mask pattern is shown in the RMC. The mask shown is made of natural cadmium and has 4 mm slits and 4 mm slats.

3.4 Neutron Source Details

The source in this research produced a poly-energetic spectrum of neutrons through the (α, n) reaction, where the source of alpha particles was a 72.7 mCi (as of 22 Sep 61) ^{239}Pu source, shown in Figure 17. The region of primary interest on the neutron energy emission spectrum is the region of neutrons below 0.5 MeV, which according to Cember only includes 3.8% of the neutrons emitted [12].

It is desirable to increase the number of thermal neutrons emitted because it would reduce the time to acquire sufficient data for a modulation profile that can generate an accurate image. One way to increase the thermal neutrons would be to thermalize the

peak neutrons through some moderating material. Although moderating the source would soften the emission spectrum, no moderation was used because it would make the source appear to the RMC to be as large as the size of the moderator. At far distances, a larger size may still appear point-like; but, at the close distances implemented in the lab, the larger size would add too much complexity to the image reconstruction.

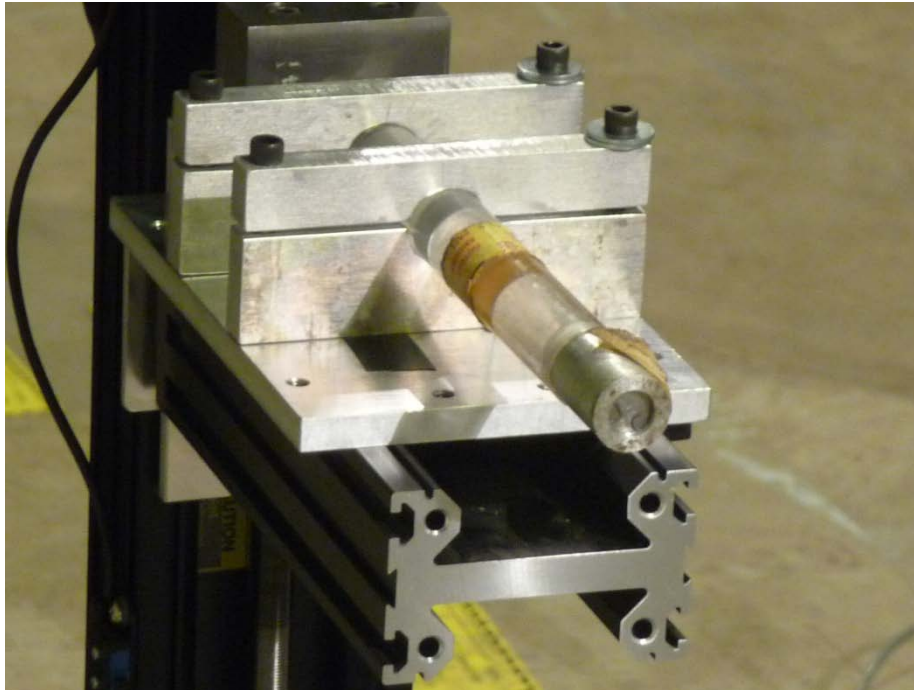


Figure 17: Pu-Be Neutron Source in Mount. The source is a 72.7 mCi Pu-Be source. The sealed source is the metallic cylinder at the end of the plastic rod that is clamped to the support stand.

3.5 Simulation of RMC in MCNP

MCNP can simulate important physics principles very precisely, but that does not indicate that the results accurately describe what would really happen in a real physical experiment. The results are only as good as the physics that are incorporated in its model

and the fidelity of the model. The latest version of the MCNP code available is MCNP5. The quality of the results depends upon the physics being modeled and the number of particles. Interpretation of MCNP results is done in statistical manner. The relative error of the results is compared to a standard range. If the relative error is below 0.1 the MCNP manual says that the results are “generally reliable” [13]. The relative error gives a measure of how the MCNP results differ with changing particles, not how the results differ from real experiments.

In MCNP, the results are in the form of a tally. Several different kinds of tallies can be used. In this research, the primary tallies that were used were the surface current tally subdivided into directional bins and energy bins and the volumetric flux tally subdivided into energy bins. The number of particles to run in a model was determined by repetition until the statistics were sufficient. The variance reduction technique of not tracking a particle once it got below .001 eV (10^{-9} MeV) was also incorporated. Other variance reduction techniques are available if desired.

3.6 Experimental Procedures Chapter Summary

This chapter has covered the experimental procedures that were used in the experiments. The RMC setup and calibration was covered along with the MCNP modeling capabilities along with the energy window settings for the ^3He and BF_3 detectors. Initial setup of the RMC is very important in the analysis of the results. Without a correct understanding of the source location with respect to the RMC, the analysis of the results would be offset by an unknown amount. The mask designs and the

source used were also described. The specific experiments were based upon the procedures described in this chapter.

IV. Results and Analysis

4.1 Chapter Overview

This chapter presents the specific settings for the experiments and the observed results followed by the analysis. It begins with the feasibility studies and then goes into the experiments that were conducted followed by the problems that became evident through the research. The BF_3 and ^3He detectors were used with Cd and Borated-Epoxy masks. The reason for the uncertainty in the results is determined to be overwhelming contribution of fast neutrons caused by downscatter and stream-through detection. Simulations were performed to determine the contributions of the fast neutron components.

4.2 Mask Feasibility Simulation

In order to validate that the mask material would moderate the incoming neutron radiation, a series of Monte Carlo simulations were run. Models for 0.025 eV (thermal), 24 keV, and 1 MeV neutrons were simulated using the prototype RMC design with 0.5” borated epoxy masks. These simulations tracked the number of particles entering the detector volume but did not account for interactions in the detector itself.

The MCNP model actually consisted of 180 separate MCNP input cards which only varied by the rotation angle of the masks. The transmitted neutrons were determined at each rotation angle by the use of the surface current (F1) tally in MCNP5. The modeled source was a neutron point source emitting a single energy, which could be defined as monoenergetic. The number of particles run in the simulations for sufficient

statistics was determined to be 10,000,000 to achieve 1% uncertainty. The result of the MCNP runs were a number of separate files that were then processed to extract the result of the surface current tally and rotation angle for the simulation. The analysis is performed using a Fortran code developed by Kowash to extract out the tally results for each rotation angle, and then a Matlab code for plotting the extracted data.

The modulation profiles for the three energies using a 1.27 cm (0.5 inches) mask are shown in Figure 18. The data is normalized to show the relative modulation efficiency of each scenario. Note that at lower source energies the modulation profile is more pronounced because of the higher boron-neutron cross section at these energies.

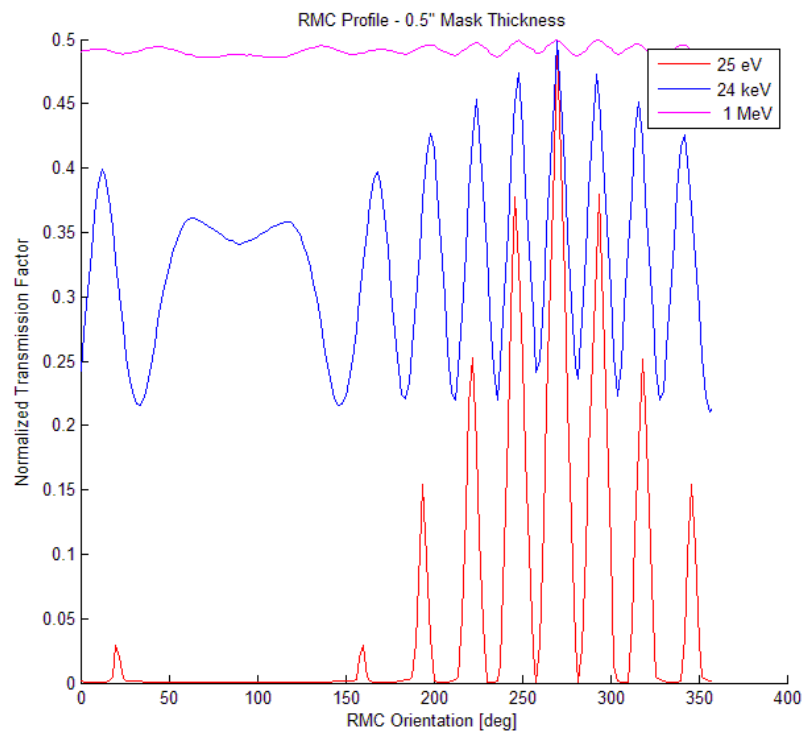


Figure 18: Normalized Modulation Profiles. The surface current tally (MCNP5-F1) was used as the result for a series of simulations that measured the number of neutrons that passed through the masks at each rotation angle.

The result of the MCNP mask feasibility simulation indicated promising results. The modulation profile was well defined and clearly pronounced. A number of areas showed the masks attenuating the neutrons to nearly nothing. The relative error was below 0.1 for each tally, and there were no warnings about the statistics not passing the 10 tests. It was not possible to determine the accuracy of the simulation because the sources used in the experiments were not monoenergetic sources.

Another MCNP model was constructed to determine how a thin layer (0.08 cm) of natural cadmium would perform as a mask material. The model again consisted of a monoenergetic (0.025 eV) neutron source. The modulation profile was generated using a different model for each rotation angle. The resulting modulation profile, in Figure 19, shows that the thin layer of cadmium has very good modulation that nears the ideal performance.

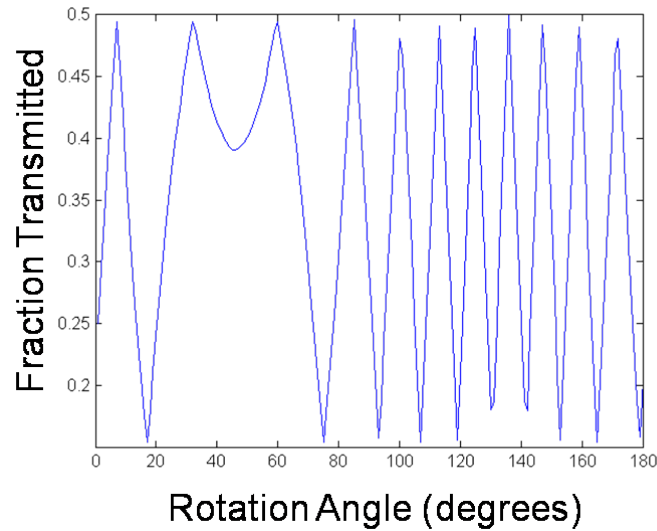


Figure 19: MCNP Generate Modulation Profile for Cadmium. The source is monoenergetic 0.025 eV neutrons and the mask is 0.08 cm thick. The modulation profile shows that the modulation is very good and close to ideal.

4.3 Mask experiment

A quick test of the attenuation of cadmium was performed before making the masks. A BF_3 detector was placed on the table that holds the RMC, which was about 2.3 meters away from the source. The detector was in a direct line of sight with the source, so only air would attenuate and scatter the neutrons. However, neutrons would also scatter off other objects in the environment like the floor, ceiling, and walls. The count rate was determined without the mask material in front and then again with the mask material blocking the radiation. The count rate was measured over a time of 100 seconds without the cadmium in front and averaged 9 counts per second (cps). A solid sheet of $1/32^{\text{nd}}$ inch thick cadmium was placed in front of the detector and the count rate was again measured over 100 seconds: The average count rate was 4 cps. That showed an attenuation of over 50%. Although the attenuation was not perfect, it was thought to be

sufficient for the modulating material. The MCNP simulations showed nearly 100% attenuation with cadmium, so there was a discrepancy between the simulation and the actual experiment. An explanation for the difference is that the MCNP model only accounted for monoenergetic neutrons and when the mask and detector were subjected to a distributed neutron flux the amount of modulation was decreased over the energy range.

4.4 Simulation of RMC Performance

By using a code, developed in Matlab for RMC image reconstruction by Kowash [3], it is possible to simulate the modulation profile and the image reconstruction. The simulation takes the fidelity variables into account and simulates the RMC performance. The closer the fidelity variables match the actual experiment, the better the simulated results match the actual results. The simulated results give a prediction of best case performance because not all of the sources of variation are included [14]. In the simulation, the energy-dependent attenuation parameter of the masks was not known or modeled accurately. The simulated results indicated that the RMC performance would be sufficient to generate images with low uncertainty. The simulated modulation profiles and image reconstructions for a source located at $(15 \pm 0.5 \text{ cm}, 15 \pm 0.5 \text{ cm})$ are shown in Figure 20. The source location in the image reconstruction is stated as Cartesian coordinates on the plane that the source can move in. The origin, or $(0,0,z)$ location, on the plane is the location where it intersects with the centerline of the RMC. The uncertainty of the reconstructed image locations is $\pm 1 \text{ cm}$. The reconstructed image

shows the source location to be $(15 \pm 1 \text{ cm}, 15 \pm 1 \text{ cm})$. The anticipated best case image reconstruction is to correctly place the source with minor uncertainty.

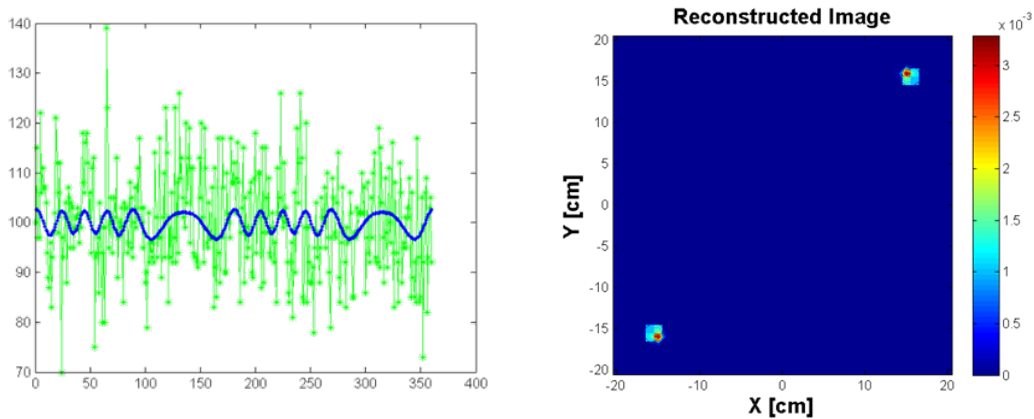


Figure 20: Simulated RMC Performance. Simulated results for a point source at $(15 \pm 0.5 \text{ cm}, 15 \pm 0.5 \text{ cm})$. Top: The simulated modulation profile illustrates the ideal modulation profile without stochastic noise with an overlay of the statistically varying modulation profile. Bottom: The simulated reconstructed image came out at $(15 \pm 1 \text{ cm}, 15 \pm 1 \text{ cm})$ and had an ambiguity at $(-15 \pm 1 \text{ cm}, -15 \pm 1 \text{ cm})$.

4.5 RMC Setup with BF_3 Detector and Cadmium Masks

The calibrated RMC setup was used with cadmium masks and the coupled BF_3 detectors. The pulse processing was setup with the analog setup to send a count to the custom LabVIEW control VI when a pulse height was within a window. Signals from the five detectors were fed into a custom summing box before the preamplifier. The same settings for the energy window apply, but the lower level discriminator needed to be changed. In this case, it was found that the motor induced a noise signal into the energy window and distorted the counts. Luckily, the noise did not overlap a substantial portion of the pulse-height spectrum, so the lower level discriminator on the PSA/T-SCA

could be set just above the noise without substantial loss to the efficiency of the counts. The lower level discriminator was set at 0.51 V, which was just above the noise caused by the motor. The output of the PSA/T-SCA was a logic pulse that was connected to both a counter and sent into the NI PCI-6111 acquisition card through the counter pin on the SCB-68. The counter module served as the check and verification that the digital counter was working properly. The count was read into the LabVIEW control VI, which also acquired the rotation angle from the angular position decoder. Therefore, a modulation profile was generated of the neutron absorption counts versus the rotation angle.

A modulation profile was recorded over a 3 hour time period for the source located at $(10 \pm 0.5 \text{ cm}, 0 \pm 0.5 \text{ cm})$ on the source plane with the RMC centerline being the origin. The image was reconstructed using the MLEM algorithm and bootstrap resampling method developed by Kowash. The results for the 3 hour run, shown in Figure 21, locate the source at $(10 \pm 6\text{cm}, -1 \pm 6\text{cm})$. This result is encouraging, but the uncertainty needs to be reduced before the method can be used with confidence.

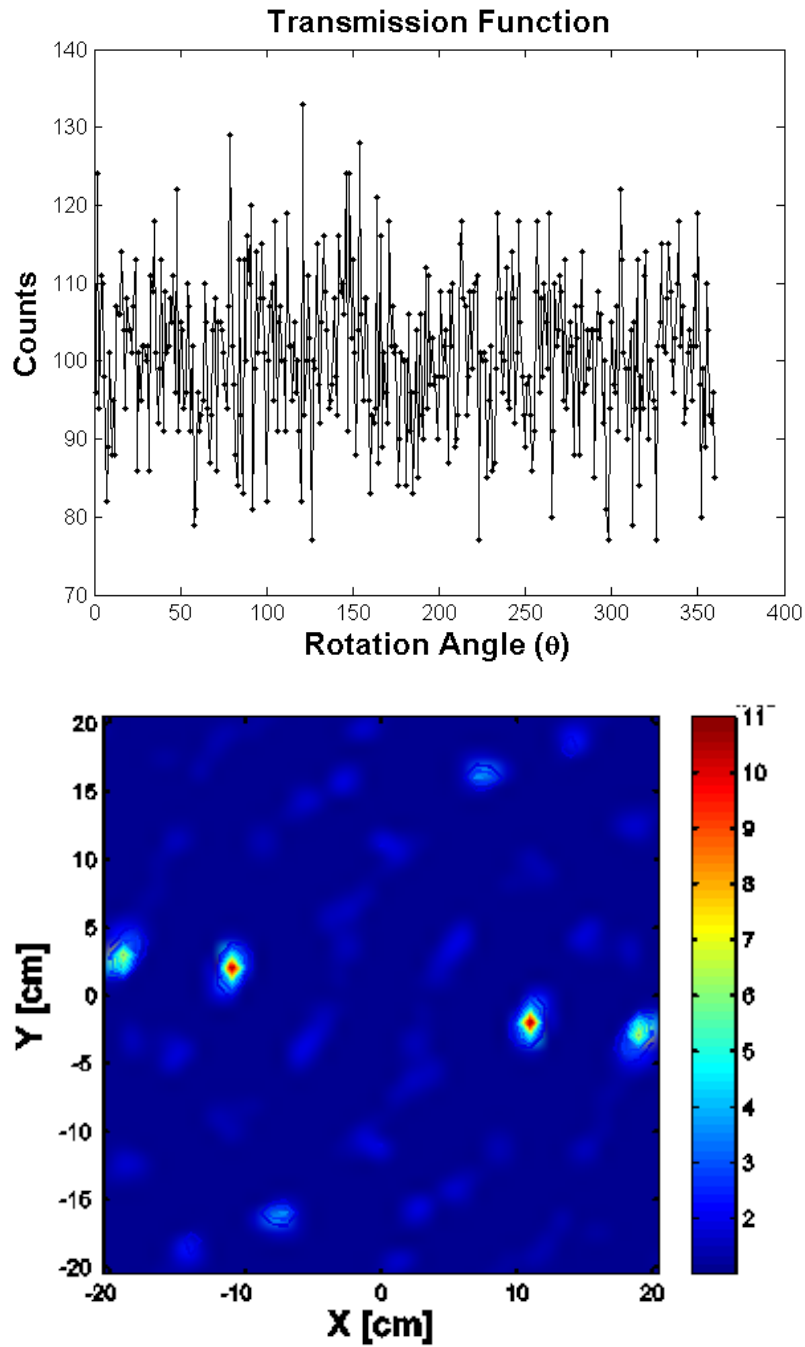


Figure 21: Measured BF_3 Modulation Profile and Image Reconstruction. The measured results for a 3 hour run with the known source position at $(10 \pm 0.5\text{cm}, 0 \pm 0.5\text{cm})$. Top: The modulation profile showing the number of detected counts for each rotation angle of the masks. Bottom: The reconstructed image obtained by running the MLEM algorithm on the measured modulation profile. The reconstructed source location was $(10 \pm 6\text{cm}, -1 \pm 6\text{cm})$.

4.6 RMC Setup with ^3He detector and cadmium masks

To determine if the ^3He detectors could also generate an image, the set up was modified for the ^3He detectors. Imaging runs were completed using the same calibrated RMC setup but with ^3He detectors inside the cadmium detector housing and the settings on the NIM modules adjusted to bracket the pulse-height spectrum for thermal neutron capture of the ^3He detector – Everything else about the RMC was the same.

The source was moved to another position and a modulation profile was recorded for three hours. The modulation profile was then used to reconstruct the source location. The modulation profile and reconstructed image are shown in Figure 22. The known source location was $(15 \pm 0.5 \text{ cm}, 15 \pm 0.5 \text{ cm})$ and the reconstructed source location was $(13 \pm 6 \text{ cm}, 12 \pm 6 \text{ cm})$. Again, the uncertainty was significant but the reconstructed location was close to the true source location.

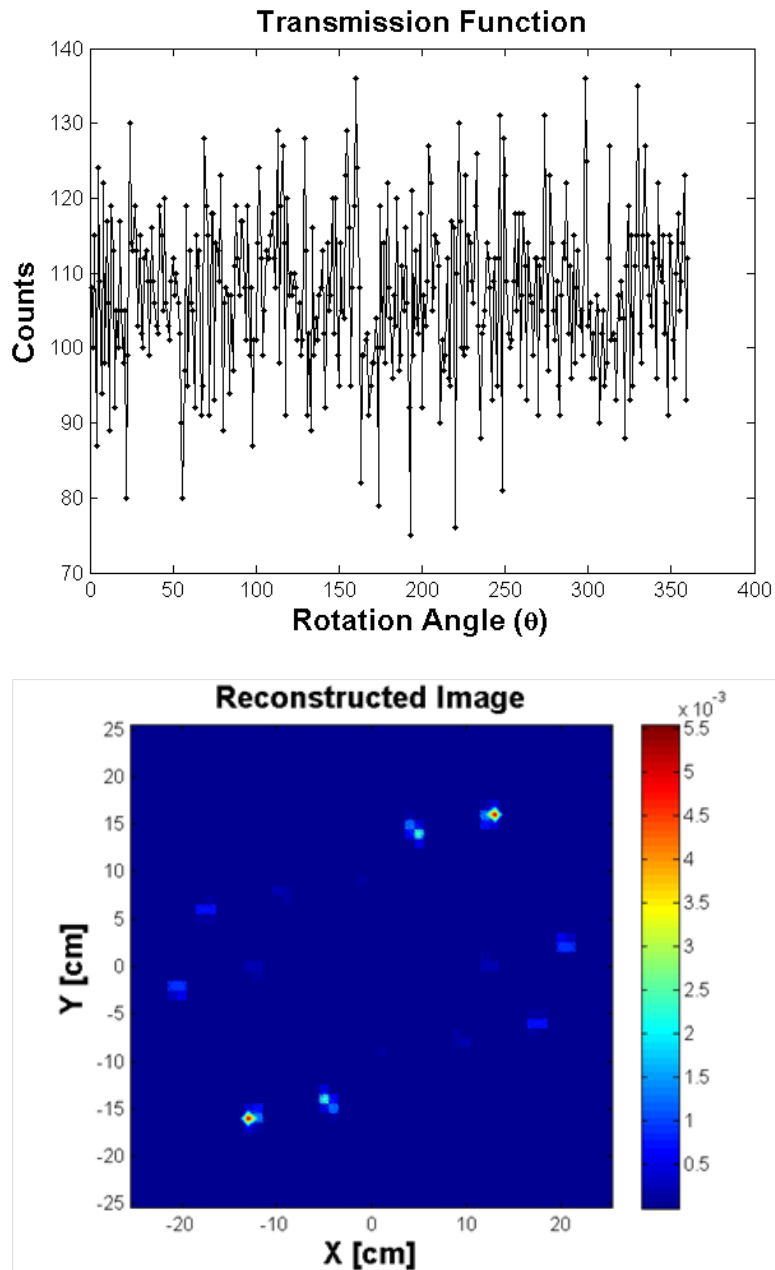


Figure 22: Measured ^3He Modulation Profile and Image Reconstruction. The measured data from a three hour run with the source at known location (15 ± 0.5 cm, 15 ± 0.5 cm). Top: The measured modulation profile showing the low modulation in the signal. Bottom: The reconstructed image showing the reconstructed source location at (13 ± 6 cm, 12 ± 6 cm).

4.7 RMC Setup with ^3He detector and Borated-Epoxy masks

The RMC masks were replaced with the half inch thick borated epoxy masks described earlier. To replace the masks it was necessary to realign the masks and recalibrate the rotation angle to enable accurate image reconstruction. Remember the home position is used in the image reconstruction algorithm. With the recalibrated RMC, 3 hour measurement times were used with the ^3He detector. It was difficult to reconstruct the images correctly most of the time, but there was one time that the image came out at approximately the right location, shown in Figure 23, with a similar uncertainty as previously. The borated-epoxy mask performance did not match the simulation. The known source position was $(10 \pm 0.5 \text{ cm}, 0 \pm 0.5 \text{ cm})$. The reconstructed image was located at $(12 \pm 5 \text{ cm}, 4 \pm 4 \text{ cm})$.

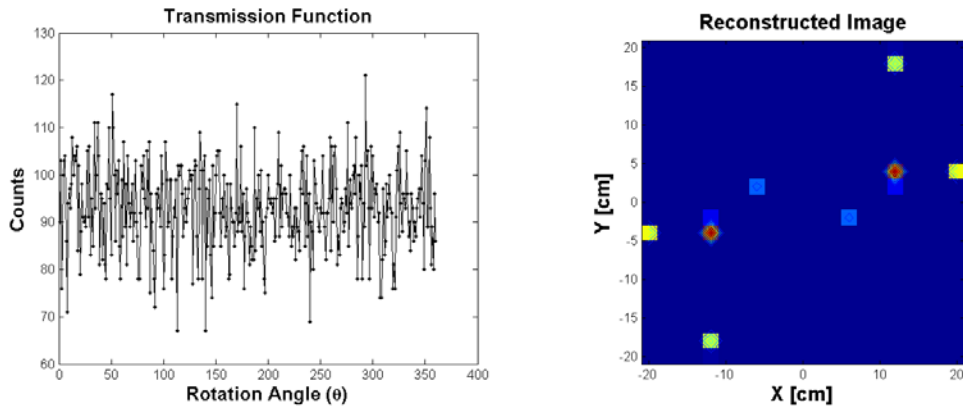


Figure 23: ^3He with Borated-Epoxy Masks. The known source position was $(10 \pm 0.5 \text{ cm}, 0 \pm 0.5 \text{ cm})$. Top: The recorded modulation profile for a three hour measurement. Bottom: The reconstructed image was located at $(12 \pm 5 \text{ cm}, 4 \pm 4 \text{ cm})$.

4.8 Distribution of Resampled Images

The Bootstrap resampling technique reconstructed distinct point sources, but the locations varied so much that the sample standard deviation was 6 cm. Because of the 180 degree ambiguity, sometimes the location of point-source was 180 degrees off: Only one side was used. To determine the distribution of the image reconstructions from the resampled data, an image reconstruction was performed on a measured modulation profile for a source at $(10 \pm .5 \text{ cm}, 0 \pm 0.5 \text{ cm})$ with 10,000 iterations of Bootstrap resampling. The location of the greatest intensity in each reconstructed image was used as the location for the point-source. Figure 24 illustrates the spread of the reconstructed locations along with the number of counts at each location. Three interesting features appear. The first is that the maximum peak, or the most frequent occurrence (11 cm, 1 cm), was near the true source location. A second feature is that the centralized peaks that appear just above and below the maximum peak appear to be reconstructed correctly in the radial component, but were slightly off in the angular component. This problem could indicate that a weighting function may be helpful to increase the influence the dip in the modulation profile has in the image reconstruction. The third feature is the that the reconstructed images that were clearly in the wrong spot (based on distance from the true source location) seem to form a ring around the most frequent occurrence. The implication of the third feature is that the algorithm creates *ghost* images in a circular pattern out from the source.

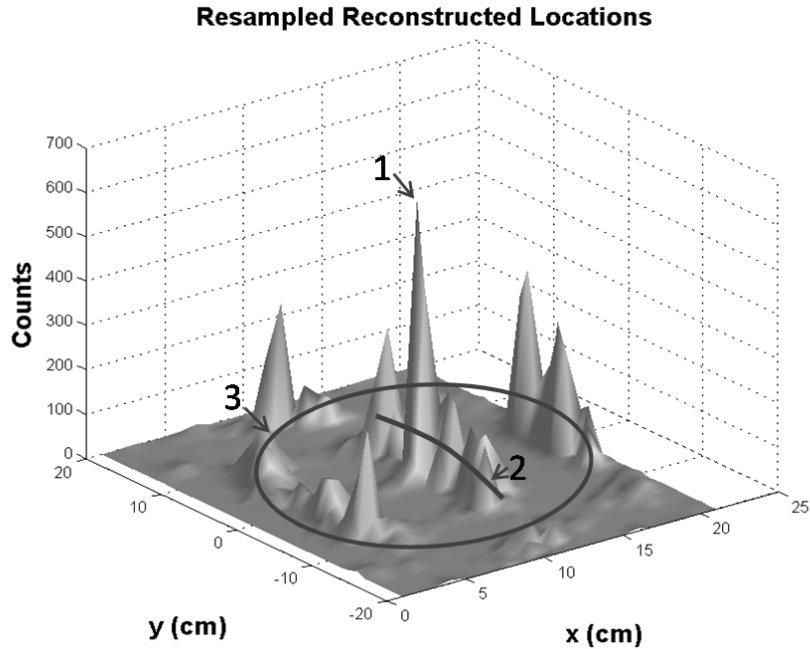


Figure 24: Resampled Reconstructed Locations. This plot illustrates the number of occurrences for the locations of the resampled point source image reconstructions. Three main features are present: 1) the maximum peak is almost exact for the known location of the source, 2) the peaks just above and below the maximum peak appear to have the radial component correct, but were slightly off on the angular component in the reconstructed location, and 3) the other peaks seem to appear in a ring around the maximum peak value in such a way that may indicate a implication with the algorithm.

4.9 Energy Distribution as Source of Uncertainty

The source of the significant uncertainty in the results of the series of experiments with both the BF_3 and the ^3He detectors needed to be identified. The poor modulation made it more difficult for the MLEM algorithm to reconstruct the source location. The Matlab simulation of the modulation profile also showed minimal modulation, but the MLEM algorithm was able to reconstruct the source location accurately and with little uncertainty. (Recall that the simulation had both an ideal modulation profile and a noisy

modulation profile. The MLEM algorithm used the noisy modulation profile data to reconstruct the simulated source location.) The measured modulation in the modulation profile was different than anticipated from the simulated results of MCNP, which had showed a clear modulation profile. The source in the MCNP simulation model was monoenergetic, whereas the source for the measurement experiment was a distribution of energies. Therefore, to better understand the mask attenuation performance in the presence of multiple energies it was determined to look at the mask influence on a multi-energetic neutron flux.

4.9.1 Downscattered vs Blocked.

The masks influence the radiation flux by either absorption or scattering. If the radiation is absorbed it will not enter the detector, but if the radiation is scattered it still could enter the detector. A collision causes a decrease in energy of the scattered radiation along with its change in direction. So, when a neutron scatters in the mask, it transfers some of its energy to the atoms it collided with inside the mask, and it leaves the mask in a different direction that could still enter the detector. With reduced energy, the downscattered neutron has a higher probability of detection. The initial feasibility MCNP simulations showed that the masks do stop the low energy radiation entering the detector. Yet there are still higher energy neutrons that downscatter in the mask with the effect of increasing the thermal neutron counts. So, the distribution of energies brought a problem of increased thermal neutrons exiting the mask. There is a tradeoff between the number of neutrons absorbed in the material and the number of neutrons downscattered into the energy window of interest. If it were possible to model the difference between

the number of neutrons stopped in the mask and the number of neutrons that were downscattered into the thermal neutron region, then that would be a good measure of the performance of the mask.

A series of MCNP simulations were performed to determine the change in the energy distribution as it passed through the mask materials, as well as the flux in the detector. The model was designed to determine the downscatter that occurred in the masks. Therefore the mask material was modeled as solid sheet as thick of the mask. An angle-sensitive, energy-binned surface current tally was used to determine the number of neutrons entering and leaving the plate of mask material. A cosine card was also used to isolate the neutrons entering from the side the source was on and leaving in the direction of the detector. Energy bins were setup to determine the number in each energy bin. A single run was performed where the energy source was a poly-energetic source. The source was placed in a vacuum and given a direction vector straight into the center of the cadmium layer. The result is shown in Figure 25, and shows the difference between the energy distribution that entered the mask material and the energy distribution of the neutrons that exited the mask material. The noticeable feature of this plot is that there are more neutrons leaving the mask at lower energies. This plot does not provide a noticeable origin for these neutrons. There is a slight dip in the faster neutrons, shown in Figure 26. Because it is shown on a log scale, it is a lot more than it seems and the lower energy neutrons are coming out in greater numbers. These results show the evidence of downscatter in the mask material through the increase in thermal neutrons after the mask.

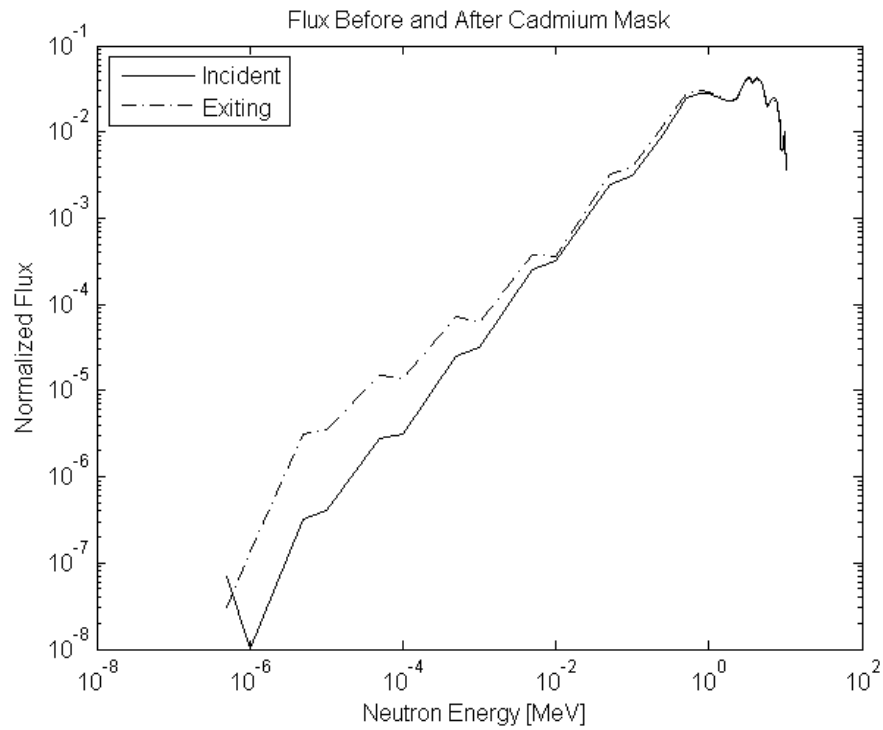


Figure 25: Downscatter in 0.08 cm Natural Cadmium. The multi-energetic neutron source simulation from MCNP is used for this plot. The energy is values are shown per energy bin. The noticeable feature of this plot is that there are more neutrons leaving the mask at lower energies. The source of these neutrons is not very noticeable in this plot. There is a slight dip in the faster neutrons that is on a log scale so it is a lot more than it seems and the lower energy neutrons are coming out in greater numbers.

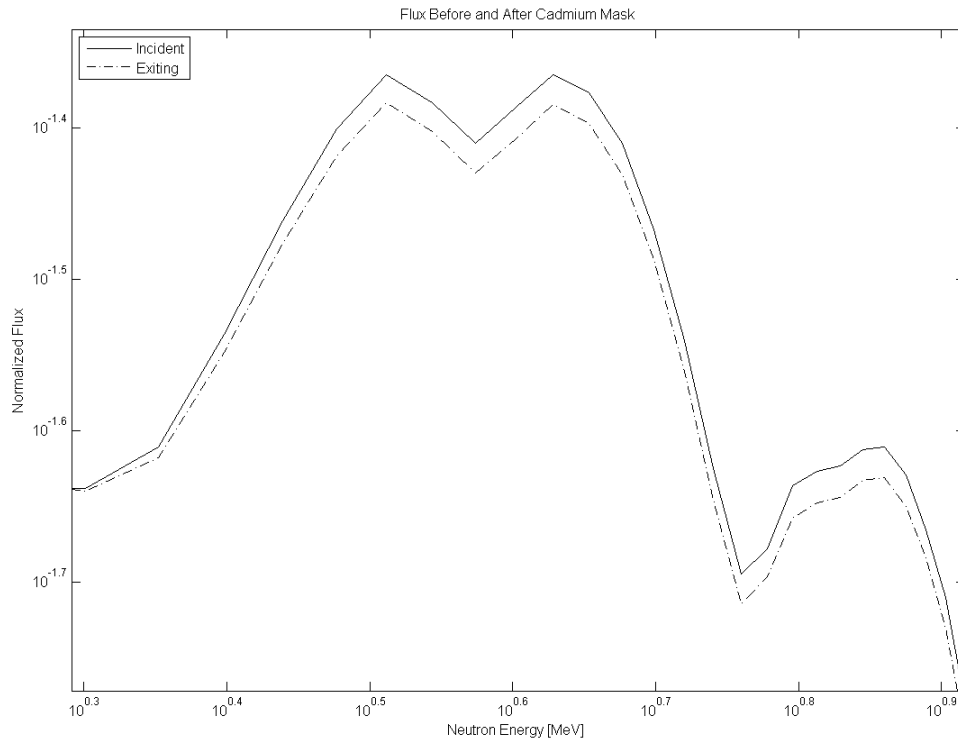


Figure 26: Zoomed in on Fast Neutron Downscatter in 0.08 cm Natural Cadmium. The number of neutrons leaving the masks is lower than the number that is incident upon the masks. The decrease in counts is desired in a mask, but the decrease in the faster region causes the increase in the thermal region, where the detector is more efficient, that was shown in Figure 25.

4.9.2 Sandwich Mask Designs.

In an attempt to improve the mask design, adjustments to the mask composition were made. The main idea of a cadmium sandwich mask was to place cadmium on each side of a moderating material to scrub out the lower energy neutrons and the neutrons in the cadmium resonance energies before reaching the moderator and then cut off the thermal neutrons after the moderating material. This would work if the cadmium were able to cut out the neutrons that are downscattering into the thermal energy regions. The

borated epoxy layer was 1.27 cm thick and had 0.08 cm cadmium layers on each side. The change in flux results are shown in Figure 27, and indicate that the resonance in the cross section of cadmium does not wipe out the energies of the neutrons that downscatter to a lower energy that is more easily detected.

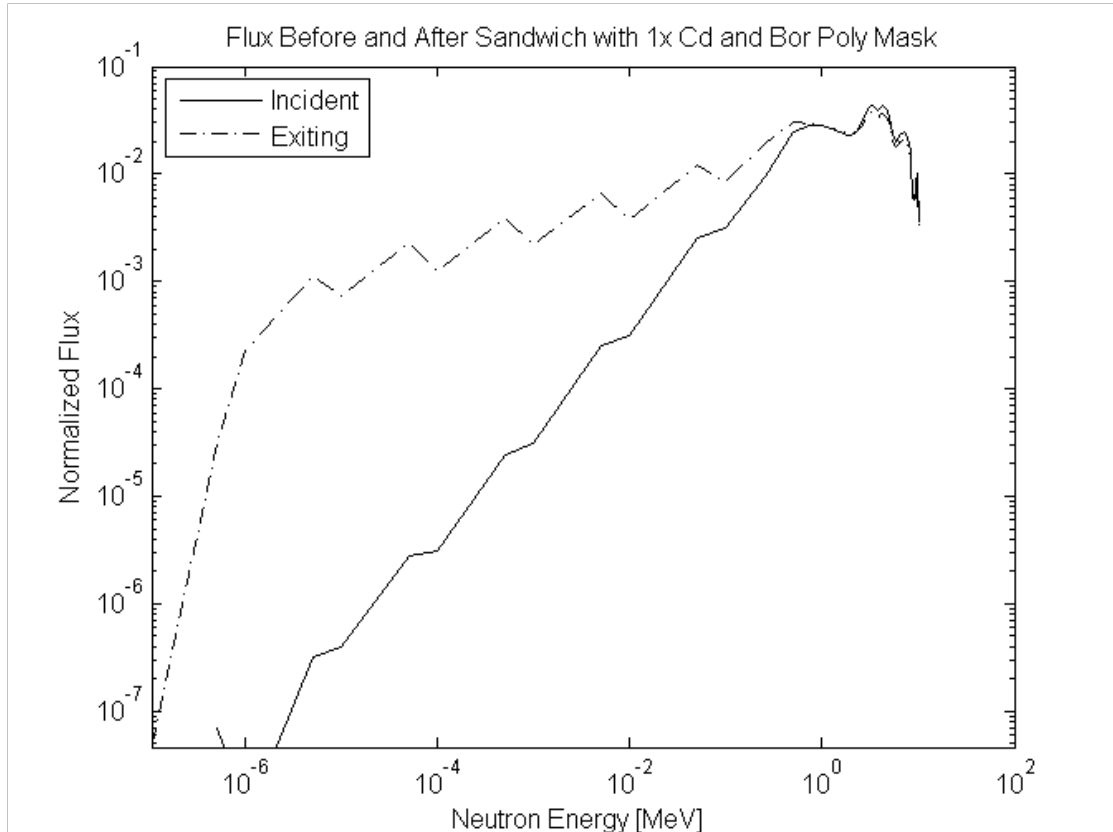


Figure 27: The Change in Flux with a Cd-BoratedEpoxy-Cd Sandwich Mask. The borated epoxy layer was 1.27 cm thick and had 0.08 cm cadmium layers on each side. The thermal components of the flux increased.

4.9.3 High Energy Neutrons Streaming Through the Masks and Being Detected.

Another potential reason for the large uncertainty is due to background counts that come from higher energy neutrons streaming through the mask or shielding and still

being detected in the detector. The mean free path for the neutrons increases as the energy increases, which means that, on average, higher energy neutrons travel farther in a medium before interacting. Therefore, for relatively thin masks, higher energy neutrons may not even interact with the masks. Some higher energy neutrons will interact because there is still a probability of interaction, even though it is small. The inverse of the mean free path is the probability of interaction. Once the neutron has passed through the masks without interaction it then has a probability of interacting in the detector. The reaction-of-interest in the detector is absorption rather than not interacting. The probability of a fast neutron being absorbed, and therefore detected, is several orders of magnitude lower than a thermal neutron being absorbed. So, it would seem that this thought could be discarded without a significant problem. Yet, a concern arises from the reaction rate calculation of equation (1.4), which indicates that the rate that neutrons of a specific energy are absorbed in the detector is the macroscopic absorption cross section multiplied by the volumetric flux in the detector. Figure 28 shows the flux, as obtained from the downscatter MCNP simulations, increases by a similar order of magnitude as the probability of absorption. The product of the two components indicates that the rate of higher energy absorption in the detector may compare to the rate of thermal neutron absorption. Because it is impossible to determine the energy of the neutron at the time of the absorption, the sum of the reaction rates over the energies as in equation (1.5) gives a better measure of mask performance.

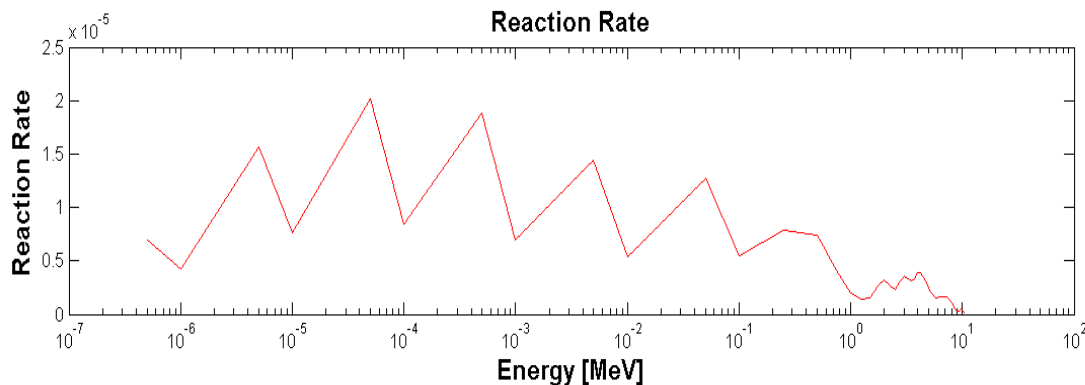
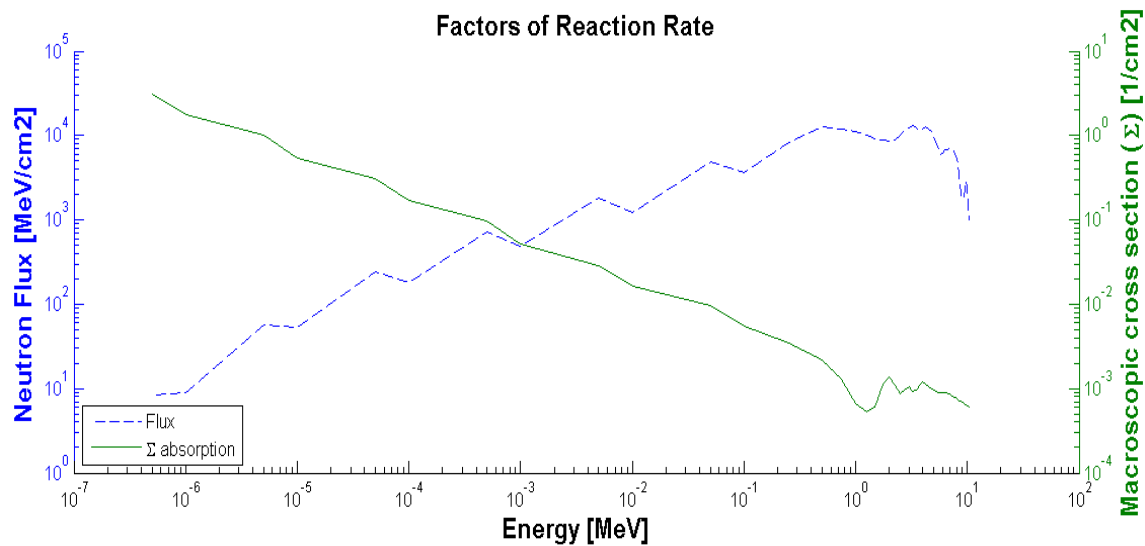


Figure 28: Reaction Rate Calculation Terms and Value. Top: Although the probability of interaction in the detector decreases by several orders of magnitude as the energy increases, the flux increases by several orders of magnitude over the same energy increase. Bottom: The reaction rate shown in normalized per source particle because the MCNP tally result is per source particle.

4.9.4 Simulation for Reaction Rate of Multi-energetic neutron source.

Because of experimental results, it was desirable to determine what effect the distribution of neutron energies had upon the reaction rate and therefore the modulation

profile. The MCNP simulations for downscatter also tallied the reaction rate, using an F4 tally with a multiplier card. The multiplier card was specified to obtain the neutron absorption reaction rate. No measures were taken to eliminate neutron absorptions that were absorbed because of thermalization in the detector. It was assumed that those reactions would be minimal. The reaction rate was determined for the cadmium mask material from the downscatter simulation, but needed to be determined when there wasn't a mask. Without the mask, the normalized reaction rate was 3.1×10^{-4} absorptions per source particle. With the cadmium mask the reaction rate did drop down to 3.0×10^{-4} absorptions per source particle. The rough calculation to get the reaction rate in counts per second could be done by multiplying the absorptions per source particle by the number of neutrons emitted in one second. The borated epoxy material resulted in a 3.9×10^{-4} absorptions per source particle.

A comparison was done for various mask designs using the total normalized reaction rate. The same MCNP simulations were used to measure the neutron absorption reaction rate for other masks and no masks. The simulation without a mask was used as a reference for the open configuration of the masks. The reaction rates for various mask materials reflect the performance of the masks when they are closed. The results are shown in Table 2. The Cd masks were the only design that lowered the total reaction rate, but the other masks designs increased the total reaction rate. The MLEM algorithm should still be able to reconstruct an image as long as there is a difference (whether increased or decreased). The reaction rate is a better indicator of measurement than the flux.

Table 2: Comparison of Total Normalized Reaction Rate for Mask Designs. The difference between no mask and the specific mask reflects the difference open and closed regions of the masks. Cadmium masks were the only masks that showed a decrease in the total reaction rate from no masks, whereas the others increased. As long as there is a difference, the MLEM reconstruction algorithm should still be able to reconstruct the image location.

Mask	Total Normalized Reaction Rate
None	3.1×10^{-4} neutrons per source particle
Cd	3.0×10^{-4}
Borated Polyethylene	3.9×10^{-4}
Cd-BorPoly-Cd	3.7×10^{-4}

4.10 Summary

Results of specific experiments have been presented and analyzed in this section. The initial MCNP mask feasibility experiment showing that both cadmium and borated-epoxy masks should create sufficient modulation for a monoenergetic neutron source. The initial experiments to test the MCNP simulations showed a reduction in counts when the mask material was in front of the detector compared to counts without mask material. The BF_3 and ^3He detectors were shown to have preliminary results with significant uncertainty. The reason for the uncertainty was the poor modulation in the modulation profile. The analysis determined that the poor modulation was a result of the overwhelming influence of the fast neutron component in the neutron flux. The downscatter of the fast neutrons increased the number of thermal neutrons. Also the reaction rate of the fast neutron detection was similar to the reaction rate of the thermal neutrons because of the larger flux of fast neutrons relative to the thermal neutrons.

Simulating the reaction rate of neutron absorption in the detector is a better method of simulation for the modulation profile.

V. Conclusions and Recommendations

5.1 Chapter Overview

This chapter describes the conclusions of the research and the recommendations for refinement in future research. This research concludes that the RMC is potentially feasible to image neutron sources using the neutrons emitted in the thermal energy. Simulations have demonstrated feasibility for monoenergetic neutron sources and experimental tests have verified that ^3He and BF_3 detectors will work in the RMC. The uncertainty in the results is caused by the higher-energy neutrons. Future work should include development of RMC components that are suitable for imaging fast neutrons. Other areas for future research involve using multiple energy windows for imaging and digitizing the pulse processing components.

5.2 Conclusions of Research

The conclusions from the research is that the RMC can potentially be modified to image thermal neutron sources but currently the images have too much uncertainty. Initial MCNP simulations indicate the masks made from cadmium and masks made from borated epoxy should produce a sufficiently modulated modulation profile for monoenergetic neutron sources at 24 keV and below. The test at 1 MeV neutron energy showed that it produced some modulation, but not very defined. The ^3He and BF_3 detectors are able to sufficiently detect thermal neutrons, but currently the uncertainties prevent the RMC from being field ready. The results are preliminary and are encouraging for future work using the RMC to image neutron sources. Due to the unforeseen significance of fast neutron interactions in both the masks and the detector,

the RMC concept has not been demonstrated to the level predicted. The distribution of neutron energies in the flux caused the masks to perform worse than simulated because the faster neutrons were not used in the simulations. The two main challenges of the fast neutron components in the source energy distribution are 1) downscattering of higher energy neutrons into lower energy regions, and 2) fast neutrons streaming through the masks without interacting, yet interacting in the detector. The conclusion from the research is that the RMC can potentially be used to image neutron sources, if the neutron energy distribution is accounted for in the selection of RMC components.

5.3 Significance of Research

The research is significant because, to the authors understanding, it has not been previously attempted to use an RMC to image neutrons of any energy. The research has initiated the work and discovered challenge areas. From this research it should be possible to continue to improve the results of the imaging system and demonstrate the feasibility of using the RMC to image neutron sources.

5.4 Recommendations for Future Research

The areas of research that are recommended for future research include fast neutron imaging, spectroscopic energy imaging, and DPP for comprehensive data collection and processing. The fast neutron imaging is recommended because most of the neutron sources that one would be searching for would have a fast neutron component, and the background for fast neutrons would be lower than it is for thermal neutrons because they do not interact as much with the environment. Eventually the three areas of future research would come together to get an imaging system that can increase the

confidence of source identity and location. When multiple modulation profiles reconstruct the neutron source at the same location then it would provide greater confidence in the source location. Another aspect that could provide greater confidence in source location would be to include a gamma ray modulation profile because most of the neutron sources also emit gamma ray radiation. The ideal signal processing component for a multiple energy imaging system would most likely involve using DPP to measure and record the necessary pulse information.

The DPP research has the potential to greatly increase the capability of the signal processing, but it can also take lots of time debugging. The DPP could be developed to capture every pulse, process it for radiation type and energy, and then store the key pulse information along with mask rotation angle. With all the key information for each pulse stored, it could be processed for whatever configuration that is desired. It would even be possible to develop modulation profiles that include energy spectral information. An FPGA likely accomplish such a task, but can take significant amounts of time in development.

One of the multiple-energy imaging projects that would not require any additional equipment would be to using both the input counters on the NI-6111 PCI card. The two counters could give two energy windows, and therefore two modulation profiles for the imaging system with only slight modifications to the RMC. Two energy windows could allow two modulation profiles and two separate image reconstructions. If the detector used is capable of distinguishing thermal and fast neutron energies, then modulation profiles could be generated for thermal neutrons and fast neutrons. Note that for image reconstruction of multiple energies, the MLEM algorithm would need to be adjusted

slightly to accommodate the changes in parameters that vary with energy, like efficiency and attenuation values. In the case of gamma ray imaging, the multiple energy windows could be set up to image two different isotope sources.

A potential area of quick performance is to use the RMC with an antimony-beryllium (Sb-Be) photoneutron source. The relatively monoenergetic-low-energies of the source would significantly reduce the effects of the fast neutrons that caused problems in the thermal research. If the measured modulation profile shows good modulation efficiency, then it would validate the conclusions made in this thesis. In obtaining and using a Sb-Be source the biological risk associated with the gamma ray source should be carefully considered and protected.

5.5 Summary

The research successfully demonstrated appropriate scientific processes toward obtaining the objective of thermal neutron imaging. The hypothesis was that with modifications made to the components of the RMC that the system could image thermal neutron sources. Simulations predicted that the system would work appropriately, but the results showed significant uncertainties. The cause of the uncertainties identified as the poor modulation resulting from the large quantity of higher energy neutrons present in the distribution. The fast neutrons blurred the modulation profiles by downscatter and stream through detection. The proposed direction is to test the current components with a neutron source that has a distribution that does not include the higher energy neutrons, or modify the components to account for the higher energy neutron flux. The next goal would be to try the setup with RMC to image fast neutron sources.

Appendix A

A.1 Liquid Scintillator Detector

Visible light is produced when radiation interacts with a scintillator material. The detection process involves sensing the prompt light emission and generating an electronic pulse. The radiation types that produce light in scintillators include both neutrons and gamma rays. The light output is generated in the de-excitation process of an electron between low energy levels to the ground state. An electron may be excited to any of the energy levels of an atom, but usually de-excites (internal conversion) without generating visible light to the single electron state. Sometimes excited singlet states can be converted into triplet states through intersystem crossing. The light output lasts longer from the triplet state than it lasts from the singlet state. Interestingly, whether the electron is excited to the singlet state or to the triplet state largely depends upon the type of radiation that causes the excitation. This principle is utilized in *pulse shape discrimination* (PSD) by analyzing the shape of the pulse to distinguish what type of radiation type caused the pulse [8]. Figure 29 shows the decay time difference from pulses of the same light output when excited by different radiation types. When pulses that are caused by different radiation types have the same light intensity, the decay component of the pulse differs by radiation type. PSD theory is based on measuring the decay components of the pulses to distinguish between the various radiation types. Alpha particles are the heaviest particles shown and the pulses that correspond to alpha particles have the longest decay components. Pulses that arise from gamma ray interactions have

the shortest decay time. Therefore, PSD makes it possible to distinguish the radiation type of pulses.

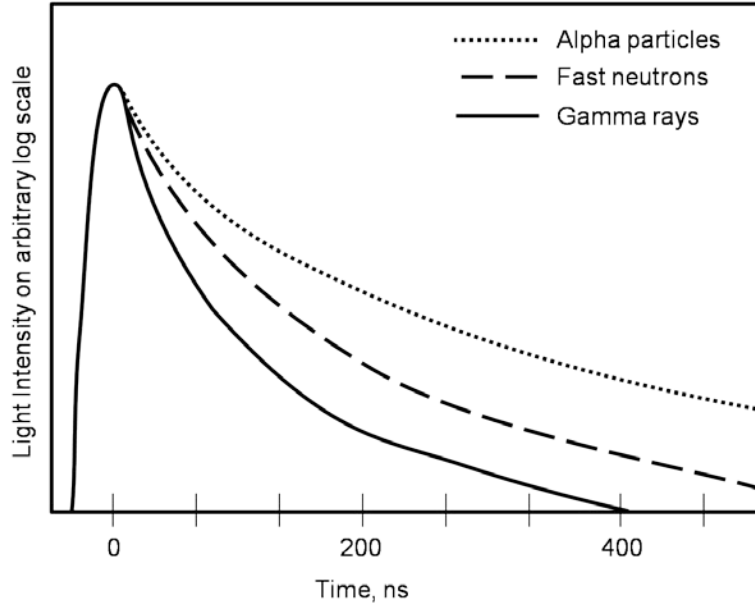


Figure 29: Decay Components for PSD. Alpha particles are the heaviest particles shown and the pulses that correspond to alpha particles have the longest decay components. Pulses that arise from gamma ray interactions have the shortest decay time. The heavier particles have a longer decay time for the same light output than the lighter particles [8].

Because the light output varies for different radiation types, the *electron equivalent energy* (eVee) unit is introduced to measure light yield on an absolute basis [8]. Hence, the eVee is not exactly a measure of energy; rather it is a measure of the light output. Therefore, a photon with incident energy of 1 MeV generates 1 MeVee light output; but, a 1 MeV heavy charged particle produces less than 1 MeVee light output.

Loaded liquid scintillators have the normal liquid, but also are loaded with an isotope or element that has a high cross section for thermal neutrons, such as boron or gadolinium. The presence of the boron or gadolinium allows them to detect thermal

neutrons. The reaction products from the neutron absorption reaction create a scintillation pulse of nearly uniform amplitude around 60 keVee [12]. If a neutron scatters enough times to thermalize within the detector, then it is possible to use the recoil pulse and the delayed capture pulse to determine the energy of the incident neutrons. This approach is called capture gated neutron spectroscopy and has been implemented by several authors [16][17].

A.2 Pulse Processing

The output voltage pulse signal of the detector is processed to determine the energy and type of radiation. The analog signal from the detector can be converted to a digital signal for digital signal processing methods that may be more accurate and repeatable. An *analog-to-digital-converter* (ADC) converts the continuous analog voltage signal into discrete voltage levels. The sampling rate determines the separation distance between the points that are sampled. The rate is determined from the specification of the ADC, but it is necessary to have a sampling rate fast enough to obtain an adequate number of discrete samples to represent the signal. The resolution of the digitized voltage is determined by the energy range of values and the number of bits in the digitizer. The resolution is determined by

$$R = \frac{E_{Range}}{2^n} \quad (1.9)$$

where n represents the number of bits in the digitizer. For example, a 12 bit digitizer and an energy range of 0-10 Volts the resolution would be 0.0024 Volts per division. The processing of the signal is often done through digital filters that can make it easier to extract the data that is desired. Digitizing the detector signal and processing it digitally is

part of a large discipline called *digital signal processing* (DSP). In nuclear pulse processing, the digital processing of pulses is often called *digital pulse processing* (DPP).

A.3 Pulse Shape Discrimination (PSD)

As mentioned earlier, the pulse shape is used to distinguish radiation type in PSD methods. The two general PSD methods are 1) rise time, or decay time, measurements and 2) altering the integration of the pulse in different ways. The rise time or decay time measurement measures the time the pulse is over a threshold. This method can be done in analog NIM bins that maintain the shape of the pulse until the decay time is measured and sent to a *Time-to-Amplitude-Converter* (TAC). The TAC converts the time between two signals to an amplitude value. The difference between the differing decay times is evident in the TAC output.

Altering the integration of the pulse to discriminate between radiation types can be done in at least two ways. The first is to split the signal into different amplifiers that vary in their shaping time setting. The different shaping times may integrate the full pulse or only a portion of it depending on how long the pulse duration is in comparison to the shaping time. The other method uses digital processing to integrate the pulse from two different starting times and then uses the ratio between the two integrals to show the difference. Pozzi demonstrated this concept for a BC-523A to discriminate between thermal and fast neutrons [17]. The neutron capture energy (around 60 keVee) associated with the thermal neutrons is close to the limit on whether it is possible to discriminate between neutrons and gamma rays [16].

The key performance metric for various methods of pulse shape discrimination between neutrons and gamma rays is the *figure of merit* (FOM) presented by Winyard in 1971. It is defined by

$$FOM_{a,b} = \frac{T}{t_a + t_b} \quad (1.10)$$

where T is the separation between the time peaks and t_a and t_b are the *full width at half maximum* (FWHM) of the corresponding time peaks [19]. PSD performance has been shown to decrease as the energy decreases [20].

A.4 Digital Equipment

The digitization process available was a National Instruments (NI) PCI-6111 card. It has several input options, but to read in an analog voltage it uses a 12 bit Analog to digital converter with a maximum sampling rate of 5MS/s. That means that it collects one sample to 12 bit accuracy every 200 nanoseconds. The digital pulse processing was performed using the PCI-6111 connected to a modified LabVIEW control VI. Although the original plan was to implement the digital pulse processing with an FPGA, the lack of time and experience dictated a change to LabVIEW. The sampling rate on the available data acquisition hardware (NI-6111) placed a limitation on the ability to process the pulses for pulse shape. The desired capability would be to have the signal generated from the detector be the input into the digital processor and be able to extract the information directly from the pulse.

A.5 PSD Implementation

The optimum method of digital PSD would be to digitize the signal from the PMT and process it quickly and store the pulse information. One approach would be to run the PMT signal into an FPGA with a fast digitizer and process the pulse real time. Using the analog digitizer available this method is not feasible because the sampling rate is not fast enough to capture sufficient pulse shape information that is required for PSD.

Another method of PSD would be to use a commercially available PSD module, like a Mesytec. Mascarenhas has successfully used the Mesytec for PSD in a fast neutron scatter camera. The performance of such a module combined with time of flight measurements was 1 false neutron count in 25,000 counts [21]. The module was custom built for the detectors used in the neutron scatter camera, but could potentially also be used in other situations with slightly lower performance. Another approach would be to use the same detector with the research; although, the detector used was not sensitive to thermal neutrons so would not work for this research. Such a commercially available module was not acquired during the research. The NI-6111 was used to read in pulses from a DLA. An illustration of the resulting pulse is shown in Figure 30. It was not sampled at a rate fast enough to capture the decay information sufficiently well to do PSD. In the energy region of interest (~60 keVee), there is not much spread in the timing information so it would require a higher resolution signal. Neither the pulse height information nor the decay time could be adequately sampled to differentiate pulse information. The pulse height reading could vary by when the signal was sampled. If it sampled it at just the right moment, then the measurement could be as good as the energy resolution of the measurement. On the other hand, if it was measured at any other time,

then the measurement would not be accurate. The decay time measurement should be taken from where the signal drops below an upper threshold and then when it drops below a second threshold. Those values could not be interpolated accurately. The NI-6111 was not sufficient fast to read a signal in and perform PSD from a single pulse.

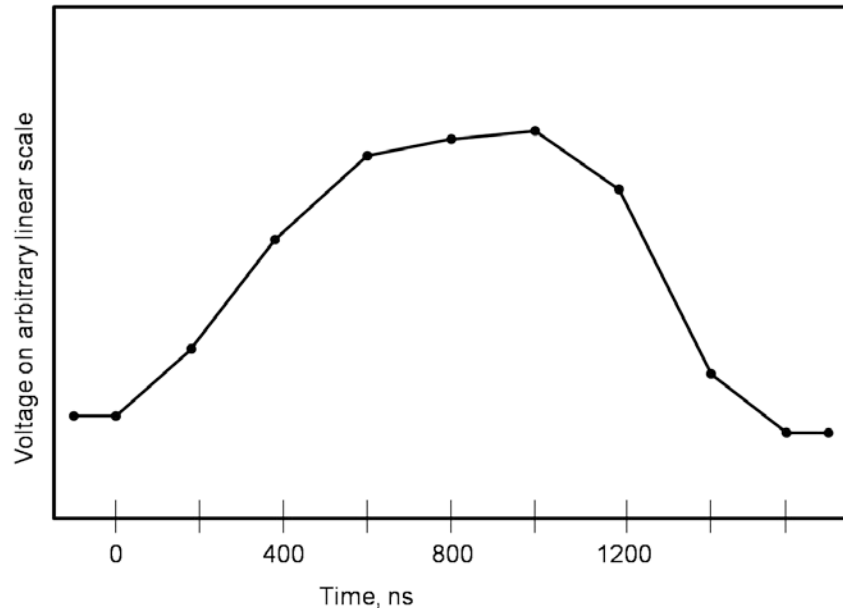


Figure 30: Illustration of Digitized Pulse from NI-6111. The sampling rate for the card was 5MS/s, so one sample every 200 ns. The pulse information is not well sampled. The peak of measurement was not stable so could alter in energy and the decay time was too fast to determine accurately where a specified percentage below the peak was located. This prevented obtaining accurate information for PSD.

Because the NI-6111 does not have a sufficient sampling rate to determine all the pulse shape information from a signal out of the PMT, then another method would be to stretch the signal until the peak can accurately be measured. One method to determine if PSD is possible with this method is to split the signal from the preamplifier and send one line into the sequence of DLA, PSA/T-SCA, and TAC while the other line is sent to a spectroscopy amplifier (and a delay amplifier to have signal from both lines arrive at the

same time). Then the NI-6111 can read in the signal from both lines through its analog input channels, as shown in Figure 31. LabVIEW can process the data for the energy window the neutron capture as well as the separation in TAC output.

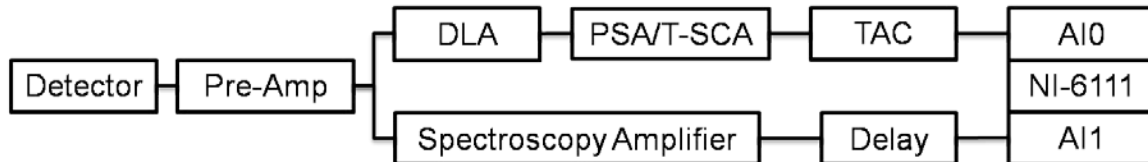


Figure 31: Instrumentation Diagram for PSD with NI-6111. The detector signal goes to a preamplifier and then the signal gets split into two lines. The top line sends a pulse whose height is the decay time of the pulse into the analog input channel 0. The bottom line sends a pulse into the analog input channel 1 where the height of the pulse corresponds to the energy of the detector. The two signals are then processed in LabVIEW to perform PSD.

The setup presented in Figure 31 should work because the peak value of the pulses would be spread out across several sampled data points. The setup was unable to be tested because of challenges in getting the TAC line to work correctly. Work in collaboration with Sandia National Lab in California demonstrated that the TAC line could work [18], but even though the NIM modules were the same, it was not demonstrated on the instruments at AFIT. The LabVIEW VI for this was only partially developed because of the time spent on the TAC line. Unfortunately the complete setup was not successfully implemented, but should have worked.

Appendix B

B.1 LabVIEW Software

LabVIEW is a software program that interfaces with data acquisition systems to receive signals and it is able to control other systems. LabVIEW creates programming modules, which it calls *Virtual Instruments* (VIs) because they perform the digitized function of an instrument. The VIs consist of a front panel and a back panel. The front panel is for input control and displaying indicators of variables. The back panel consists of the programming logic for the instrument. The programming is done in a unique graphical programming language called G [22].

B.2 Cross Section, MFP, Neutron Flux, and Reaction Rate Plotting

Matlab code that incorporated MCNP results and cross section data for isotopes [24].

```
clc;
clear all;
close all;
fig_num =1;
IsotopeXS
MCNPresults

XS = B10absorption;
%% Plot XS data
figure('color',[1,1,1])
    loglog(B10absorption(:,1),B10absorption(:,2), '.k')
    hold on
    loglog(Cdnatural(:,1),Cdnatural(:,2), 'k')
    hold on
    loglog(He3xs(:,1),He3xs(:,2), 'k--')
%     axis([1e-8, 10, -inf, inf])
axis([1e-8, 1.5e-5, -inf, inf])
xlabel('Energy (MeV)', 'fontsize',14, 'fontweight', 'b')
ylabel('Cross Section (b)', 'fontsize',14, 'fontweight', 'b')
legend('B10', 'Natural Cd', 'He3',1)

% figure(fig_num)
%     loglog(B11absorption(:,1),B11absorption(:,2))
```

```

%      fig_num = fig_num+1;

%% Call Reaction Rate Calculation function
Activity = 3.7e6

F4 = F4Tally;
Ebins = Ebins_CdMask;
N = 0.243e22; %B-10 number density for BC-523a as given by spec sheet
N = 2.254e19 % BF3 calculated
[totRR_CdMask,RR_CdMask,Macro] = RRcalc(XS,Ebins,F4,N,Activity);

%% efficiency calc
efficiencyE = 1.-exp(-Macro.*2);

figure('color',[1,1,1])
semilogx(Ebins,efficiencyE,'k')
xlabel('Energy (MeV)','fontsize',14,'fontweight','b')
ylabel('Calculated Efficiency','fontsize',14,'fontweight','b')

%%

% MCNP Flux calculations
%multiply f4 by activity
flux2 = Activity.*F4Tally;
%multiply together
RR1 = Macro.*F4Tally;
% RR1 assumes that the only neutron absorption is occurring because
of the B-10 content.
totRR1 = sum(RR1);
RR2 = Macro.*flux2;
totRR2 = sum(RR2);
MFP = 1./Macro;

figure('color',[1,1,1])
loglog(Ebins,MFP,'k')
xlabel('Energy (MeV)','fontsize',14,'fontweight','b')
ylabel('Calculated MFP (cm)','fontsize',14,'fontweight','b')

%% plot with different y axis
figure('color',[1,1,1])
subplot(6,1,[1 3])
[AX,H1,H2] = ...
plotyy(Ebins_CdMask,flux2,Ebins_CdMask,Macro,'loglog') %'semilogx')
set(get(AX(1),'Ylabel'),'String','Neutron Flux
[MeV/cm2]','fontsize',14,'fontweight','b')
set(get(AX(2),'Ylabel'),'String','Macroscopic cross section
(\Sigma) [1/cm2]','fontsize',14,'fontweight','b')
xlabel('Energy [MeV]','fontsize',14,'fontweight','b')
set(H1,'LineStyle','--')
set(H2,'LineStyle','-')
title('Factors of Reaction Rate','fontsize',14,'fontweight','b')
legend('Flux','\Sigma absorption',3)
subplot(6,1,[5 6])
semilogx(Ebins_CdMask, RR_CdMask,'r')

```

```

ylabel('Reaction Rate','fontsize',14,'fontweight','b')
xlabel('Energy [MeV]','fontsize',14,'fontweight','b')
title('Reaction Rate','fontsize',14,'fontweight','b')
%%
figure('color',[1,1,1])
    loglog(Ebins_CdMask, MFP) %Macro
    hold on
    loglog(Ebins_CdMask, 10,'k')
    title('MFP in BF3 Detector')
    xlabel('Energy [MeV]')
    ylabel('MFP [cm]')
    hold off

figure('color',[1,1,1])
    %semilogx(Ebins_CdMask,flbefore_CdMask,'b')
    loglog(Ebins_CdMask,flbefore_CdMask,'k')
    hold on
    %semilogx(Ebins_CdMask,flafter_CdMask,'r')
    loglog(Ebins_CdMask,flafter_CdMask,'-.k')
    title('Flux Before and After Cadmium Mask')
    xlabel('Neutron Energy [MeV] ')
    ylabel('Normalized Flux ')
    legend('Incident', 'Exiting',2);

figure('color',[1,1,1])
    loglog(Ebins_BPMask,flbefore_BPMask,'k')
    hold on
    loglog(Ebins_BPMask,flafter_BPMask,'-.k')
    title('Flux Before and After Borated Polyethylene Mask')
    xlabel('Neutron Energy [MeV] ')
    ylabel('Normalized Flux ')
    legend('Incident', 'Exiting',2);

figure('color',[1,1,1])
    loglog(Ebins_sand1,flbefore_sand1,'k')
    hold on
    loglog(Ebins_sand1,flafter_sand1,'-.k')
    title('Flux Before and After Sandwich with 1x Cd and Bor Poly
Mask')
    xlabel('Neutron Energy [MeV] ')
    ylabel('Normalized Flux ')
    legend('Incident', 'Exiting',2);

%adjust for different Ebins
figure('color',[1,1,1])
    loglog(Ebins_sand1,flbefore_sand1,'k')
    hold on
    loglog(Ebins_CdMask,flafter_CdMask,'-.k')
    hold on
    loglog(Ebins_BPMask,flafter_BPMask,'--.k')
    hold on
    loglog(Ebins_sand1,flafter_sand1,'r')
    title('Flux Before and After Masks')
    xlabel('Neutron Energy [MeV] ')

```

```

ylabel('Normalized Flux ')
legend('Incident', 'Cd Mask', 'Bor Poly Mask', 'Sandwich Mask', 2);

% Reaction Rates
figure('color',[1,1,1])
loglog(Ebins_CdMask,F4m_CdMask,'k')
hold on
loglog(Ebins_BPMask,F4m_BPMask,'-.k')
hold on
loglog(Ebins_sand1,F4m_sand1,'--.k')
hold on
loglog(Ebins_noMask,F4m_noMask,'r')
title('Reaction Rates')
xlabel('Neutron Energy [MeV] ')
ylabel('Reaction Rate ')
legend('Cd Mask', 'Bor Poly Mask', 'Sandwich Mask', 'No Mask', 4);

%% total Reaction Rate Calculations
totRR_noMask = sum(F4m_noMask)
totRR_CdMask = sum(F4m_CdMask)
totRR_BPMask = sum(F4m_BPMask)
totRR_sand1 = sum(F4m_sand1)

```


Appendix C

C.1 Electronic Settings for Thermal Neutron Energy Window

The voltage signal from the detector needed to be processed to determine the radiation type and energy. In the tube detectors used in this research, the gamma rays were discriminated against by using an energy window where only voltage pulses whose peak value was within the range of values of the window were counted. The specific settings for BF_3 and ^3He detectors were different. Each window is described in this section. The purpose of the windows was to enable accurate counting of neutron absorption, which most likely corresponds to thermal neutrons.

C.1.1 Settings for BF_3 Detector.

The energy window that was set up was intended to select the pulse heights that corresponded to the neutron capture reaction. The energy window was determined by sequentially verifying the signal at each module in the Nuclear Instruments Module (NIM) bin electronics process to make sure that it worked as anticipated. In the end, the window needed to be adjusted to eliminate a noise signal originating from the RMC motor that could not be eliminated in any other way. A detector was placed near the neutron source to increase the count rate to determine the settings for the NIM bin modules, which are shown in Table 3. For BF_3 detectors, the counting plateau was determined to be between 1100 and 1400 volts, so a 1200 V bias was used. The output of the detector was sent to a preamplifier, and then to the amplifier, which was an Ortec 671. The amplification helps separate the signal from the noise that is in the line, but even low amplitude noise is amplified as well as the signal. The course gain was 20 and

the fine gain was 1.5. Other settings were a 2 μ s Gaussian shaping time with auto base line restoration (BLR). The signal was sent from the amplifier to the Ortec 552 PSA/T-SCA. For this purpose the PSA/T-SCA was only used for an energy window. The lower level discriminator was set to 0.23 V. The upper level discriminator was set to 1.21 V, but it did not matter because the detector operated in integral mode. The energy window that was set up in this way was intended to window in on the pulse heights that corresponded to the neutron capture reaction.

Table 3: Settings for BF₃ Analog Setup. The settings for each module are displayed in this table. The signal goes from the preamplifier to the amplifier to the PSA/T-SCA and then into the counter to be sent to LabVIEW.

Module	NIM Module	Setting	Value	Units
Preamplifier	Ortec 142	None	N/A	N/A
Amplifier	Ortec 671	Course Gain	20	N/A
		Fine Gain	1.5	N/A
		Shaping Time	2	μ s
		Mode	Gaussian	N/A
		BLR	Auto	N/A
		Input	Positive	N/A
PSA/T-SCA	Ortec 552	Upper Level	1.21	Volts
		Lower Level	0.23	Volts
		Mode	Integral	N/A
		B-Fraction	N/A	N/A
		Attenuation	x1	N/A
PCI Card	NI-6111	Input Counter	N/A	N/A

C.1.2 Settings for ³He Detector.

The energy window for the ³He detector was determined in the same way that the energy window for the BF₃ detector was found. The counting plateau for the ³He detectors was found to be 1500 volts. The settings for the preamplifier, amplifier, PSA/T-SCA, and PCI input card are shown in Table 4. The amplifier was set to 2 μ s

shaping time with a course gain of 100, and a fine gain of 1.5. The lower level discriminator for the PSA/T-SCA was set to 0.42 V and the upper level was set to 0.71 V. This energy window corresponded to the epithermal peak in the energy spectrum caused by the absorption of the neutrons.

Table 4: Settings for ^3He Energy Window. The ^3He detector settings are different for than the BF_3 because of the lower energy values associated with the reaction.

Module	NIM Module	Setting	Value	Units
Preamplifier	Ortec 142	None	N/A	N/A
Amplifier	Ortec 671	Course Gain	100	N/A
		Fine Gain	1.5	N/A
		Shaping Time	2	μs
		Mode	Gaussian	N/A
		BLR	Auto	N/A
		Input	Positive	N/A
PSA/T-SCA	Ortec 552	Upper Level	0.71	Volts
		Lower Level	0.42	Volts
		Mode	NORM	N/A
		B-Fraction	N/A	N/A
		Attenuation	x1	N/A
PCI Card	NI-6111	Input Counter	N/A	N/A

Appendix D

D.1 Photoneutron Reaction Sources.

Photoneutron sources are nearly monoenergetic neutron sources resulting from using a radioisotope gamma ray source in conjunction with an appropriate target material. Knoll indicates that only two practical isotopes exist for photoneutron sources: Either ${}^9\text{Be}$ or ${}^2\text{H}$ isotopes [8]. The energy at which the neutron is emitted is determined by

$$E_n(\theta) \cong \frac{M(E_\gamma + Q)}{m + M} + \frac{E_\gamma \left[(2mM)(m + M)(E_\gamma + Q) \right]^{\frac{1}{2}}}{(m + M)^2} \cos(\theta) \quad (1.11)$$

where theta (θ) is the angle between the gamma ray and neutron direction, E_γ is the gamma ray energy, M is the mass of the recoil nucleus times the speed of light squared, and m is the mass of the neutron also times the speed of light squared [8]. The range of the neutron emission energy from specific gamma energy is calculated by taking the maximum and minimum values of theta. If the gamma source is relatively monoenergetic, then the energy distribution of the neutrons produced would also be nearly monoenergetic [8]. Although photoneutron sources would appear to be an ideal neutron source for neutron proof-of-concept imaging, one problem is the need for a source of high energy gamma rays with a high activity to produce sufficient neutron fluxes. Because of the combination of penetrating high energy gamma rays and a large source activity, the gamma ray source would be a biological concern for the experimental setup [10]. An Sb-Be photoneutron source that would emit monoenergetic 22 keV neutrons was considered for the research, but was not procured in the available time.

Bibliography

- [1] Oda, M. "High-Resolution X-Ray Collimator with Broad Field of View for Astronomical Use," Applied Optics, vol. 4, no.1, p.143, Jan 1965.
- [2] Mertz, L. "A Dilute Image Transform with Application to an X-Ray Star Camera," Symposium on Modern Optics, Polytechnic Institute of Brooklyn, p 787-791, Mar 1967.
- [3] Kowash, B.R. A Rotating Modulation Imager for the Orphan Source Search Problem, Ph.D. Dissertation, University of Michigan. September 2008.
- [4] Hurford, et.al., "The RHESSI Imaging Concept". Kluwer Academic Publishers. 2002.
- [5] Sharma, A.C. "Development and Design of a High-Energy Gamma Camera for Use with NSECT-Imaging: Feasibility for Breast Imaging," IEEE Trans. Nucl. Sci., vol. 54, no. 5, p 1498-1507, Oct 2007.
- [6] Barrett, H.H. and Myers, K.J. "Foundations of Image science". Wiley, New York, 2004.
- [7] Sharma, A. et al. "Near-field high-energy spectroscopic gamma imaging using a rotation modulation collimator." Nucl. Inst. & Meth B 266 (2008) 4938–4947.
- [8] Knoll, Glenn F. "Radiation Detection and Measurement, 3rd Edition". Wiley, New York, 2000.
- [9] AF NETF Graphite Standard Pile, USAF Technical Report NO. WADD-TR-61-174, March 1962.
- [10] Shultis, J.K. and Faw, R.E. "Radiation Shielding". American Nuclear Society. 2000.
- [11] Chart of Nuclides. Korea Atomic Energy Research Institute (KAERI), accessed Dec 2009, Available: <http://atom.kaeri.re.kr/>
- [12] Cember, H. "Introduction to Health Physics, 3rd edition." McGraw-Hill, New York, 1996.
- [13] Monte Carlo N-Particle Transport Code System, Version 5, Release 1.51, Radiation Safety Information al Computation Center, Oak Ridge, TN, January 2009.

- [14] Boyce, N.O., Kowash, B.R., Wehe, D.K. “Thermal Neutron Imaging with a Rotating Modulation Collimator.” Proceedings of IEEE NSS/MIC 2009 Conference Record.
- [15] Spears, “Characterizing a neutron energy spectrum using a “Forward Edge” neutron time-of-flight spectroscopy technique”, AFIT Master’s Thesis, 2005.
- [16] Frey, Wesley D. “Use of BC-523A liquid scintillator for simultaneous neutron spectroscopy and gamma counting with the implementation of a neutron history reconstruction algorithm.” Oregon State University PhD dissertation, March 6, 2009.
- [17] Flaska, M. and Pozzi, S.A. “Digital pulse shape analysis for the capture-gated liquid scintillator BC-523A”. Nucl. Inst. & Meth. A. 17 October 2008.
- [18] Personal Correspondence with Nick Mascarenhas and others at Sandia National Lab. Jan 2010.
- [19] Winyard, et al. Nucl. Instrum. & Meth. 95 (1991) 141.
- [20] Heltsley, et al. Nucl. Instrum. & Meth. A 263 (1988) 441.
- [21] Marleau, P. et al. “Advances in Imaging Fission Neutrons with a Neutron Scatter Camera.” Proceedings of IEEE NSS 2007 Conference Record.
- [22] National Instruments. “LabVIEW Professional Development System – version 8.2”. National Instruments. 2006.
- [23] National Instruments PCI-6110/6111 Specifications. Accessed: Nov 2009. Available: <http://www.ni.com/pdf/manuals/370980a.pdf>
- [24] Matlab 2009a. The MathWorks. 2009.

REPORT DOCUMENTATION PAGE				<i>Form Approved OMB No. 074-0188</i>	
The public reporting burden for this collection of information is estimated to average 1 hour per response, including the time for reviewing instructions, searching existing data sources, gathering and maintaining the data needed, and completing and reviewing the collection of information. Send comments regarding this burden estimate or any other aspect of the collection of information, including suggestions for reducing this burden to Department of Defense, Washington Headquarters Services, Directorate for Information Operations and Reports (0704-0188), 1215 Jefferson Davis Highway, Suite 1204, Arlington, VA 22202-4302. Respondents should be aware that notwithstanding any other provision of law, no person shall be subject to a penalty for failing to comply with a collection of information if it does not display a currently valid OMB control number. PLEASE DO NOT RETURN YOUR FORM TO THE ABOVE ADDRESS.					
1. REPORT DATE (DD-MM-YYYY) 25-03-2010		2. REPORT TYPE Master's Thesis		3. DATES COVERED (From - To) May 2009 - Mar 2010	
4. TITLE AND SUBTITLE Thermal Neutron Point Source Imaging using a Rotating Modulation Collimator (RMC)				5a. CONTRACT NUMBER	
				5b. GRANT NUMBER	
				5c. PROGRAM ELEMENT NUMBER	
6. AUTHOR(S) Boyce, Nathan O., 2d. Lt., USAF				5d. PROJECT NUMBER 09ENP155	
				5e. TASK NUMBER	
				5f. WORK UNIT NUMBER	
7. PERFORMING ORGANIZATION NAMES(S) AND ADDRESS(S) Air Force Institute of Technology Graduate School of Engineering and Management (AFIT/EN) 2950 Hobson Way, Building 640 WPAFB OH 45433-7765				8. PERFORMING ORGANIZATION REPORT NUMBER AFIT/GNE/ENP/10M-01	
9. SPONSORING/MONITORING AGENCY NAME(S) AND ADDRESS(ES) Defense Threat Reduction Agency CSU ATTN: COL Mark Mattox 1900 Wyoming Blvd SE Kirtland, AFB, NM 87117-5669				10. SPONSOR/MONITOR'S ACRONYM(S) DTRA/CSU	
				11. SPONSOR/MONITOR'S REPORT NUMBER(S)	
12. DISTRIBUTION/AVAILABILITY STATEMENT APPROVED FOR PUBLIC RELEASE; DISTRIBUTION UNLIMITED.					
13. SUPPLEMENTARY NOTES					
14. ABSTRACT This thesis demonstrates a previously untested capability of the Rotating Modulation Collimator (RMC) to image a point-like neutron source. The encouraging results, achieved using low-energy neutrons, provide motivation for further refinement and continued research with higher-energy neutrons. The detector and the masks on an existing RMC imaging system were exchanged to function with neutrons. The source in this research produced a poly-energetic spectrum of neutrons through the reaction. The source of alpha particles was a 72.7 mCi 239Pu source. The RMC detector was located 250 cm from the bare source and operated for three hours to generate a modulation profile: The number of particles detected at each rotation angle of the masks - it is unique for each source location. The measured modulation profiles were used in a Maximum-Likelihood-Expectation-Maximization algorithm to reconstruct the images, and a Bootstrap resampling technique was used to determine uncertainty. The reconstructed images exhibited high contrast but low precision. The resampled image locations were widely distributed, but the most frequent value was very accurate. The uncertainty originated from an expectation model that did not account for fast neutron downscatter into the thermal neutron region as well as the fast neutrons streaming through the masks and being detected.					
15. SUBJECT TERMS Neutron Imaging, Rotating Modulation Collimator (RMC), Neutron Detection					
16. SECURITY CLASSIFICATION OF:			17. LIMITATION OF ABSTRACT	18. NUMBER OF PAGES	19a. NAME OF RESPONSIBLE PERSON
a. REPORT	b. ABSTRACT	c. THIS PAGE			19b. TELEPHONE NUMBER (Include area code)
U	U	U	UU	102	Benjamin R. Kowash, Capt., USAF (937) 255-3636, ext 4571 (Benjamin.Kowash@afit.edu)

Standard Form 298 (Rev. 8-98)
Prescribed by ANSI Std. Z39-18